# Gradient Sensing by a Bistable Regulatory Motif Enhances Signal Amplification but Decreases Accuracy in Individual Cells

Rati Sharma[1], Elijah Roberts[1*]


[1] Department of Biophysics, Johns Hopkins University, Baltimore, Maryland 21218, USA

[*] Corresponding author.
Email: eroberts@jhu.edu (ER)

Short title: Accuracy During Single-Cell Gradient Sensing

**Abstract**

Many vital eukaryotic cellular functions require the cell to respond to a directional gradient of a signaling molecule. The first two steps in any eukaryotic chemotactic/chemotropic pathway are gradient detection and cell polarization. Like many processes, such chemotactic and chemotropic decisions are made using a relatively small number of molecules and are thus susceptible to internal and external fluctuations during signal transduction. Large cell-to-cell variations in the magnitude and direction of a response are therefore possible and do, in fact, occur in natural systems. In this work we use three-dimensional probabilistic modeling of a simple gradient sensing pathway to study the capacity for individual cells to accurately determine the direction of a gradient, despite fluctuations. We include a stochastic external gradient in our simulations using a novel gradient boundary condition modeling a point emitter a short distance away. We compare and contrast three different variants of the pathway, one monostable and two bistable. The simulation data show that an architecture combining bistability with spatial positive feedback permits the cell to both accurately detect and internally amplify an external gradient. We observe strong polarization in all individual cells, but in a distribution of directions centered on the gradient. Polarization accuracy in our study was strongly dependent upon a spatial positive feedback term that allows the pathway to trade accuracy for polarization strength. Finally, we show that additional feedback links providing information about the gradient to multiple levels in the pathway can help the cell to refine initial inaccuracy in the polarization direction.

## 1 Introduction

Chemotaxis and chemotropism in response to a signaling gradient are fundamental aspects of eukaryotic cellular physiology [1, 2]. Eukaryotic cells are thought to detect and polarize along even a shallow gradient using time integration of the noisy concentration difference across the cell combined with an ultrasensitive response [1]. Determining the capacity for eukaryotic pathways to extract information from signaling gradients in the environment is important for quantitatively understanding many complex developmental processes [3].

The *Saccharomyces cerevisiae* mating pathway serves as a model system for eukaryotic polarization. Haploid yeast sense nearby cells of the opposite mating type by detecting a pheromone

2

gradient and then polarize in the direction of the gradient before forming a mating projection in an attempt to mate with the partner. For a review, see [4]. Experiments monitoring individual yeast cells in an artificial gradient show that they polarize with a broad distribution of directions centered on the gradient (see for example Figure 1H in [5] and also [6–8]). As the projection grows it gradually refines its direction to be aligned more accurately with the gradient, which is thought to be a process distinct from choosing the initial direction. It is also observed that under nonsaturating pheromone conditions the decision to polarize or not is bimodal, *i.e.*, some yeast polarize and some do not. The bistable nature of the decision to polarize is well characterized [9,10], but the probability distribution of the initial polarization direction currently has not been theoretically studied.

Polarization of a cell along a gradient involves two, possibly interconnected, processes. First, the cell must detect the direction of the gradient and create an internal gradient of an activated signaling molecule aligned to the external one. Second, the cell must significantly amplify the internal gradient relative to the weak external one. In yeast cells for example, Maeder *et al.* [11] have shown that an internal gradient of Fus3 is created in response to pheromone stimulation centered at the mating projection. For a recent review of the mechanisms of cell polarization in yeast cells, see [12]. Mathematical modeling has been used to successfully study cell polarization for many years, see [13], and many different mathematical and computational methods have been applied to the problem. For a detailed comparison of the advantages and disadvantages of the various methods of modeling cell polarization, see [14].

Many deterministic partial differential equation (PDE) models have shown that positive feedback loops can sense a gradient and orient a cell along an axis of polarization. In a modeling study of yeast bud site selection, it was shown that an autocatalytic feedback loop involving active Cdc42, Cdc24, and Bem1 results in formation of a unique site of polarization [15]. Recently, Chou *et al.* studied the ability of a polarization site to adjust its location in response to a change in the input gradient [16]. They found that multiple interconnected positive and negative feedback loops can generate a variety of dynamics, including polarization sites that track a gradient. Local excitation, global inhibition triggered excitable networks have also been shown to be capable of polarizing along a gradient, in the case of *Dictyostelium discoideum* chemotaxis [17, 18]. However, all of the above studies were performed using deterministic simulations, and as such do not

provide insight into the variability of behavior in individual cells, only the population average.

Many experimental studies have shown that cell-to-cell variability in a population does in fact give rise to important biological phenomena [19–24]. Stochastic models are thus typically employed to theoretically study the probabilistic nature of individual cells [25–30]. Altschuler *et al.* showed that positive feedback in stochastic, spatial models can give rise to switch-like behavior in time and space even without spatial cues [31]. When the density of signaling molecules exceeds a threshold, clusters of activated signaling molecules develop causing a transition from an "off" state to an "on" state [32, 33]. In a critical range of concentrations, areas of the membrane with a high density emerge during the "on" state, effectively forming clusters. These clusters define the polarization. Similar behavior in which biochemical networks transition between distinct phenotypic states has been thoroughly studied in well-stirred (non-spatial) systems exhibiting bistability under the framework of stochastic dynamical systems theory, *e.g.*, [34–46]. Polarity establishment, with or without a gradient, in stochastic reaction-diffusion systems can also be considered a result of bistability in the dynamical system [47–50]. Wave pinning is another form of spatial resolved bistability [51].

Internal amplification of an external gradient is a key outcome of polarization. In a one-dimensional model of yeast polarization, Lawson *et al.* studied polarization of Spa2 in response to a deterministic Cdc42a gradient [52]. They identified a spatial amplification effect, in which the stochastic model predicted a sharper internal gradient relative to the deterministic model. Noise caused the polarization site to fluctuate and the ensemble average of the stochastic model recapitulated the deterministic results. Their results depend upon a spatial positive feedback, ascribed to F-actin filaments. Previous evidence also suggests that F-actin structure is one element providing the spatial positive feedback during yeast polarization [53].

Although there has been some work on determining the absolute accuracy with which a cell can sense a gradient [54, 55], no work has yet been done to determine the accuracy of sensing motifs at the level of individual cells. Here, we present a study of the individual cell-to-cell variability in polarization direction produced by a model of cell polarization. We study the initial step in which the cell decides where the site of polarity will be located. We are interested in the distribution of decisions that cells make in their initial guess, before any adjustments are made. We use a three-dimensional model of a cell and a spatial, stochastic modeling method known as the

reaction-diffusion master equation (RDME) to account for probabilistic reactions and diffusion. The kinetic model consists of a membrane bound ligand receptor coupled to a phosphorylation cascade. We include accurate stochastic fluctuations in the ligand gradient modeled as a nearby point source using a new constant gradient boundary condition. We show that a bistable circuit architecture is key to achieving high amplification of shallow gradients, but that there is a tradeoff with respect to the ability of the circuit to accurately select the direction. All individual cells achieve high amplification of the external gradient, but the accuracy of polarizing along the gradient varies. The strength of the spatial positive feedback is a critical parameter in allowing sharp amplification in the bistable model.

## 2  Models and Methods

### 2.1  Spatial model

Here we describe the spatial organization of our polarization model. The simulation volume (see Fig 1a for a diagram) consists of a diffusion volume containing a point source of a ligand (L). L is produced with a rate of 865 molecules $s^{-1}$, which is typical of a single yeast cell's pheromone excretion rate [56], and diffuses with a diffusion constant of D=50 $\mu m^2 s^{-1}$. Starting at zero concentration of L, we numerically solve the time dependent diffusion partial differential equations (PDEs) for the diffusion volume. We use a linear gradient boundary condition to approximate an infinite diffusion volume (see Text S1 for details). We integrate until t=30 s and then stop the simulation to obtain the gradient produced by a cell shortly after signal initiation.

Embedded within the diffusion volume is a reaction volume containing the three-dimensional model of the responding cell. The origin of the reaction volume is (0,0,0) and the location of the point source is (-0.5,-0.5,-0.5), where all units are in $\mu m$. The reaction volume is a cube 2.5 $\mu m$ on each side. The reaction volume is further subdivided into a cubic lattice with each subvolume in the lattice having an edge length of 50 nm, resulting in a 50x50x50 lattice. For each subvolume on the boundary of the reaction volume, we calculate the mean concentration of L from the final state of the PDE simulation of the diffusion volume and this value becomes the parameter for the constant gradient boundary condition used in the spatial stochastic simulations (see Text S1). The boundary condition establishes and maintains the gradient, including the correct stochastic
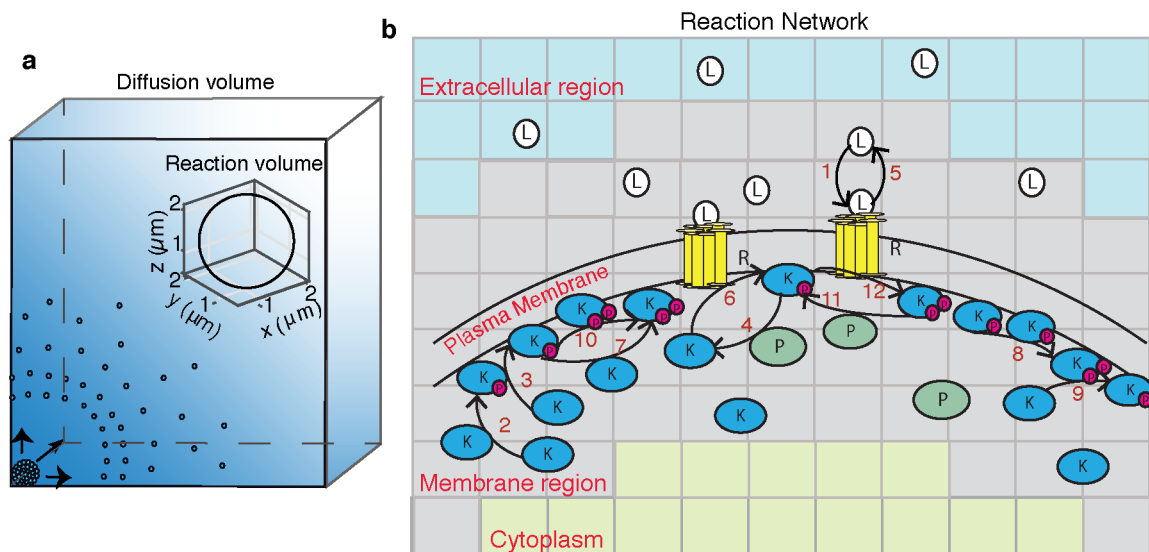
**Fig 1**: **Diagram of the simulated system.** (a) The simulation volume is composed of a diffusion volume in which the diffusion gradient of a ligand from a point source is calculated deterministically and a reaction volume in which both reaction and diffusion of the ligand and biomolecules are calculated stochastically. (b) A schematic of the processes that occur within the reaction volume. The reaction volume has three separate regions in which each molecule has distinct reaction and diffusion properties: the extracellular region, the plasma membrane, and the cytoplasm. Ligand (L) is confined to the extracellular space and can bind with a receptor (R) in the plasma membrane to form a receptor-ligand complex (RL). RL can trigger an autophosphorylation cascade of kinase (K) to the singly (Kp) and doubly (Kpp) phosphorylated states. Phosphatase (P) removes a single phosphate group from an activated kinase. See text for details.

fluctuations, in the reaction volume during the course of the simulation. The gradient across the cell goes from 16.8 nM to 12.2 nM, which is within the range required for efficient mating between yeast cells [57].

Within the reaction volume the diffusion and reaction properties of the subvolumes are manipulated to construct a physical model of a cell, including extracellular, membrane associated, and cytoplasmic subvolumes [58]. See Fig 1b for a schematic. The cell model is centered in the reaction volume and is spherical like a typical haploid yeast cell, but we have scaled the cell size down from a diameter of $\sim 4\,\mu$m to $2\,\mu$m for computational efficiency. The outer region of the reaction volume forms the extracellular space. A minimum distance of 5 subvolumes separates the boundary from the membrane of the cell. This distance is sufficient to allow any artifacts in the variance of L from the constant gradient boundary conditions to dissipate (see Text S1 for details). The spherical membrane associated region is on average 2 subvolumes thick and represents both the plasma membrane and also nearby extracellular and cytoplasmic space, to allow modeling of the

6

interaction of molecules in the plasma membrane and other regions. The interior of the spherical membrane shell contains the cytoplasmic region.

Ligand (L) molecules can diffuse in both the extracellular and membrane associated regions with D=50 $\mu$m$^2$ s$^{-1}$. When an L molecule is in the same membrane associated subvolume as a receptor (R) molecule a reaction can occur forming a receptor-ligand complex (RL). Likewise, kinase (K) molecules diffusing freely with D=5.0 $\mu$m$^2$ s$^{-1}$ in the membrane associated region can be phosphorylated into the singly (Kp) or doubly phosphorylated state (Kpp) by RL, Kp, or Kpp in the same subvolume and thus become recruited to the plasma membrane with slower D=0.005 $\mu$m$^2$ s$^{-1}$ (this value is varied later in the study). Phosphatase (P) molecules likewise diffuse freely in the membrane associated subvolumes with D=5.0 $\mu$m$^2$ s$^{-1}$ dephosphorylating Kp and Kpp molecules recruited to the plasma membrane.

## 2.2 Coordinate systems

To analyze the polarization on the membrane of the cell in response to the ligand gradient, we use two different coordinate systems. Fig 2a shows the cell in a spherical projection. The vector $\vec{r}$ is the location of the point on the membrane relative to the center of the cell. The first coordinate system uses the polar coordinate $\theta$ to specify the location of $\vec{r}$ in the x-y plane, which varies between $-\pi$ to $\pi$, and the $z$ position of $\vec{r}$ (see $\vec{r_1}$ in Fig 2a). An equirectangular projection of this coordinate system is used to show distributions on the membrane. Fig 2b shows such a projection of the ligand gradient at the membrane in the absence of reactions.

The second coordinate system is an order parameter $\Omega$, which follows concentration of L. The gradient in the cell follows the diagonal vector from (0,0,0) to (2.5,2.5,2.5). The angle the vector $\vec{r}$ makes with this diagonal is called $\Omega$ (see $\vec{r_2}$ in Fig 2a). All $\vec{r}$ vectors with the same $\Omega$ form a circle around the diagonal and by symmetry have the same L concentration in the gradient. $\Omega$ is 0 when the vector is aligned along the gradient direction and $\pi$ when the alignment is exactly opposite. Fig 2c shows the concentration of L in the membrane associated subvolumes according to $\Omega$, again in the absence of reactions.
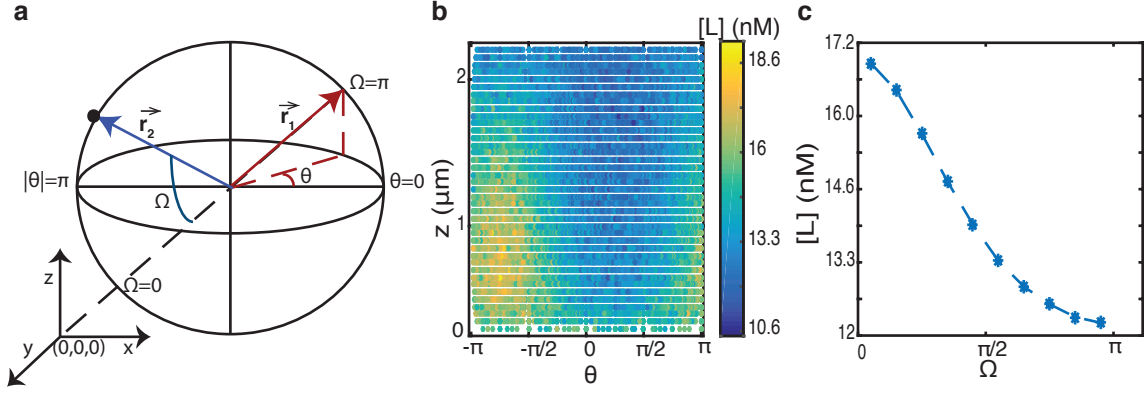
**Fig 2**: **Coordinate systems used in the analyses.** (a) A spherical projection of the modeled cell. The vector $\vec{r_1}$ (the solid red line) goes from the center of the cell to a point on the membrane. The angle of the projection of this vector on the x-y plane is labeled $\theta$, which varies from $-\pi$ to $\pi$. The z coordinate of $\vec{r_1}$ is used along with $\theta$ to make equirectangular projections of the membrane surface. An alternate coordinate system uses the angle $\Omega$ that the vector, $\vec{r_2}$ (the solid blue line), makes with the diagonal vector from (0,0,0) to (2.5,2.5,2.5), which follows the gradient. Subvolumes with the same $\Omega$ have the same ligand concentration in the gradient. $\Omega$ ranges from 0 in the highest concentration region to $\pi$ in the lowest. (b) Equirectangular projection of the ligand concentration in the membrane subvolumes. (c) $\Omega$ vs mean ligand concentration for the membrane subvolumes.

**Table 1**: Kinetic Equations

| # | Models | Reaction | Const. | Model I | | Model II | | Model III | |
|---|--------|----------|--------|---------|-----|----------|-----|-----------|-----|
| | | | | ODE | CME | ODE | CME | ODE | CME |
| 1 | I,II,III | RL → R + L | $c_5$* | 0.01 | $4.0\times10^{-3}$ | 10 | $8.0\times10^{-3}$ | 10 | $8.0\times10^{-3}$ |
| 2 | I,II,III | K + K → K + Kp | $2c_1$† | 0.01 | $4.0\times10^{-5}$ | var | $8.0\times10^{-5}$ | var | $8.0\times10^{-5}$ |
| 3 | I,II,III | Kp + K → Kp + Kp | $2c_2$† | 0.12 | $8.0\times10^{-5}$ | var | $2.32\times10^{-4}$ | var | $2.32\times10^{-4}$ |
| 4 | I,II,III | P + Kp → P + K | $c_0$† | 1 | $1.0\times10^{-3}$ | 5 | $4.0\times10^{-3}$ | 5 | $4.0\times10^{-3}$ |
| 5 | I,II,III | R + L → RL | $c_4$† | 1 | $8.0\times10^{-3}$ | 10 | $8.0\times10^{-3}$ | 10 | $8.0\times10^{-3}$ |
| 6 | I,II,III | RL + K → RL + Kp | $c_6$† | 1 | $1.0\times10^{-4}$ | 0.1 | $8.0\times10^{-5}$ | 0.1 | $8.0\times10^{-5}$ |
| 7 | II,III | K + Kp → K + Kpp | $c_1$† | – | – | var | $4.0\times10^{-5}$ | var | $4.0\times10^{-5}$ |
| 8 | II,III | Kp + Kp → Kp + Kpp | $c_2$† | – | – | var | $1.16\times10^{-4}$ | var | $1.16\times10^{-4}$ |
| 9 | II,III | Kpp + K → Kpp + Kp | $2c_3$† | – | – | 10 | $8.0\times10^{-3}$ | 10 | $8.0\times10^{-3}$ |
| 10 | II,III | Kpp + Kp → Kpp + Kpp | $c_3$† | – | – | 5 | $4.0\times10^{-3}$ | 5 | $4.0\times10^{-3}$ |
| 11 | II,III | P + Kpp → P + Kp | $2c_0$† | – | – | 10 | $8.0\times10^{-3}$ | 10 | $8.0\times10^{-3}$ |
| 12 | III | RL + Kp → RL + Kpp | $c_7$† | – | – | – | – | 0.01 | $8.0\times10^{-6}$ |

*units=dimensionless (ODE), s$^{-1}$ (CME); †units=dimensionless (ODE), molecule$^{-1}$s$^{-1}$ (CME)

## 2.3 Kinetic models

We present simulations and analyses of three kinetic models in this study. All three models are variants of the phosphorylation cascade shown schematically in Fig 1, similar to that used in previous studies [49, 50]. There are three kinase states in the system: unphosphorylated (K), singly phosphorylated (Kp) and doubly phosphorylated (Kpp). The total concentration of the kinases is kept constant. The kinases of the cascade positively regulate each other through phosphoryla-

**Table 2**: Initial Concentrations

| Species | Model I | | Models II and III | |
|---|---|---|---|---|
| | ODE$^\dagger$ | CME$^*$ | ODE$^\dagger$ | CME$^*$ |
| K | 1 | 64 | 1 | 64 |
| Kp | 0 | 0 | 0 | 0 |
| Kpp | – | – | 0 | 0 |
| P | 0.25 | 16 | 0.25 | 16 |
| R | 1.6 | 400 | 1.6 | 100 |
| L | 2 | var | 4 | var |
| RL | 0 | 0 | 0 | 0 |

$^\dagger$units=dimensionless
$^*$units=molecules/$(2.5 \times 2.5 \times 2.5 \, \mu\mathrm{m}^3)$

tion and are negatively regulated via phosphatases that dephosphorylate Kp and Kpp. Sensitivity of the cascade to the ligand is provided by the receptor-ligand complex, which is also able to phosphorylate the kinases. All of the reactions are shown in Table 1.

We carried out deterministic analyses of the three models to determine their stability, by solving the steady states for the systems of ordinary differential equations (ODEs). If the steady state solution has only one physically relevant solution, the system is considered to be monostable, *i.e.*, it has only one fixed point. As a result the system exists in only one stable steady state. If the solution gives three physically relevant solutions, it has three fixed points, two of those are stable steady state solutions and the third is an unstable state. Such a system is termed bistable. We will call the state with low concentration of phosphorylated kinase (Kp+Kpp) the "off" state and that with a high concentration the "on" state.

We also carried out a well-stirred stochastic analysis of each model using the chemical master equation (CME; see Text S1). A CME based analysis can also be used to determine mono- or bistability, but in this case one obtains more information than just the fixed points. We performed stochastic simulations to obtain the stationary probability density functions (PDFs) of each species. If the system has a unimodal distribution, it is monostable whereas, if it has a bimodal distribution, it is bistable. The stochastic simulations also give the switching times between the two meta-stable states in the case of a bistable distribution.

Table 1 gives the parameter values used in the various models and Table 2 gives the initial conditions. For simplicity during the ODE analyses, the rates and concentrations are nondimensionalized relative to the Model I dephosphorylation reaction and kinase concentration, respectively. The rates for ODE Models II and III were optimized for bistability.

*Model I.* The first model we consider is Model I listed in Table 1. The kinases in this model exist in only two forms: K and Kp. The rate equations for K and Kp as obtained from these reactions are as follows:

$$\frac{\mathrm{d}K}{\mathrm{d}t} = -2c_1 K{\cdot}K - 2c_2 Kp{\cdot}K + c_0 P{\cdot}Kp - c_6 RL_{ss}{\cdot}K, \tag{1}$$

$$\frac{\mathrm{d}Kp}{\mathrm{d}t} = 2c_1 K{\cdot}K + 2c_2 Kp{\cdot}K - c_0 P{\cdot}Kp + c_6 RL_{ss}{\cdot}K. \tag{2}$$

$RL_{ss}$ is the steady state concentration of RL complex and is obtained by setting the following rate equation to zero:

$$\frac{\mathrm{d}RL}{\mathrm{d}t} = c_4(R_0 - RL)(L_0 - RL) - c_5 RL, \tag{3}$$

where $R_0$ and $L_0$ are initial concentrations of the receptor and the ligand, respectively. Setting Eqs (1) and (2) to zero yields

$$Kp = \frac{2c_1 K^2 + c_6 RL_{ss}{\cdot}K}{c_0 P - 2c_2 K}. \tag{4}$$

Substituting Kp=1-K, P=0.25 and $RL_{ss}$ as obtained from Eq. (3) one obtains,

$$K = \frac{16(c_1 - c_2)}{-c_0 - 8c_2 - 4c_6 RLss + \sqrt{32c_0(c_1 - c_2) + (c_0 + 8c_2 + 4c_6 RL_{ss})^2}}, \tag{5}$$

which has only one positive solution. Thus, there is only one fixed point for K and Kp and the system is monostable. When Kp is plotted against ligand concentration, we see that the fraction of Kp increases smoothly with increasing ligand concentration, as shown in Fig 3a. This continuous increase in phosphorylated kinase concentration with increasing ligand concentration is also an indication of a monostable state. In biological terms, there is a graded response of the fraction of phosphorylation as ligand concentration is increased.

In the solution for the stationary PDF of the stochastic model, only a single peak exists. The mean of the PDF shifts as the ligand concentration increases, as shown in Fig 3b for three different ligand concentrations. The CME-based stochastic simulations show the same graded response to increased ligand as the deterministic model. Individual trajectories fluctuate about the fixed point, shown in Fig S1.
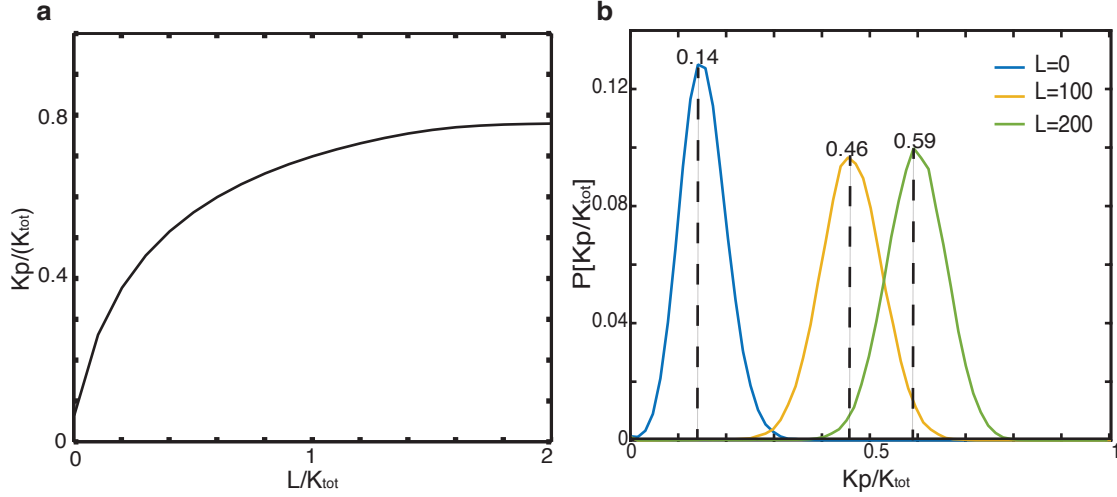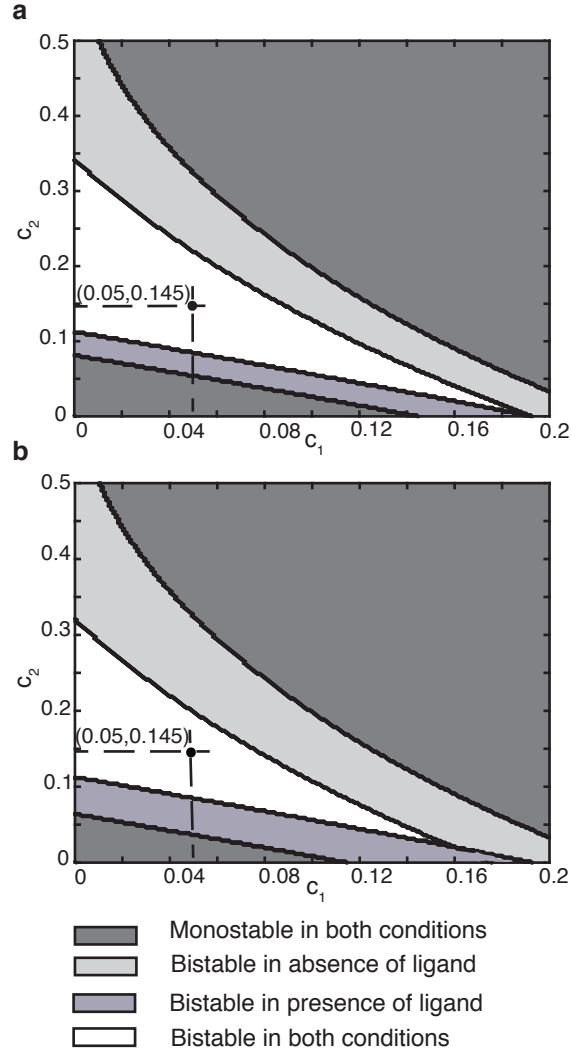
**Fig 3**: **Stability properties of Model I.** (a) A plot of the fraction of phosphorylated kinases vs ligand concentration from the deterministic solution. (b) Stationary probability density of fraction of phosphorylated kinases obtained from 100 independent stochastic simulations of Model I. Ligand copy numbers are 0 (blue), 100 (yellow), 200 (green) and the mean fraction of phosphorylated kinases for the three ligand concentrations are 0.14, 0.46 and 0.59 respectively.

*Model II.* The second model we analyze builds upon Model I, but adds a doubly phosphorylated state to the kinase (Kpp). The addition of the third kinase state in the model introduces new reactions that create Kpp from Kp and dephosphorylate Kpp back into Kp, see Table 1. The rate equations for kinases in this system are:

$$
\begin{aligned}
\frac{\mathrm{d}K}{\mathrm{d}t} &= c_0 P{\cdot}Kp - 2(c_1 K + c_2 Kp + c_3 Kpp)K - c_6 RL_{ss}{\cdot}K, \\
\frac{\mathrm{d}Kp}{\mathrm{d}t} &= (c_1 K + c_2 Kp + c_3 Kpp)(2K - Kp) - c_0 P{\cdot}Kp + 2c_0 P{\cdot}Kpp + c_6 RL_{ss}{\cdot}K, \\
\frac{\mathrm{d}Kpp}{\mathrm{d}t} &= (c_1 K + c_2 Kp + c_3 Kpp)Kp - 2c_0 P{\cdot}Kpp.
\end{aligned}
\tag{6}
$$

We can carry out deterministic analysis similar to that for Model I. Substituting $RL_{ss}$ into Eq. (6) and setting it to zero give us steady state solutions for K, Kp, and Kpp. For a small region of the parameter space three solutions exist, two of which are stable fixed points and one is an unstable fixed point, which means that the system in this regime in bistable. The remaining part where only one solution exists is the monostable regime. The various regions of the $c_1$ vs $c_2$ parameter space are shown in Fig 4a. All our simulations and analyses take place in the bistable regime, where we can efficiently simulate many switches back and forth between the "off" and "on" states.

**Fig 4**: **Stability properties of Models II and III.** Parameter space of autophosphorylation rate constants $c_1$ and $c_2$. (a) The monostable and bistable regions of Model II. (b) The monostable and bistable regions of Model III. The two marked points show the parameters selected for studying the bistable system in the stochastic models.

Stochastic simulation of Model II in the bistable regime confirms that the system is bistable in the well-stirred CME. Fig S2 shows representative trajectories and PDFs from stochastic simulations at different ligand concentrations. It is clear from the trajectories that the system is bistable when there is no ligand present, even though the stationary probability for the "on" state is low. The system makes short excursions to the "on" state. As the ligand concentration increases, the amount of time spent in the "on" state increases with a corresponding decrease in the duration

of the "off" events. But, in contrast to the graded response of the deterministic model, individual trajectories are always in either the "off" or "on" state. The systems spend no appreciable time in the intermediate region. In a population of cells this would correspond to heterogeneity in the population, with some cells "on" and other cells "off".

*Model III.*   The third model that we present in this study is a further extension of Model II. In Model III there are now two positive feedback links rather than just one, *i.e.*, in addition to all the reactions in Model II, there is one additional reaction in which the RL complex can also convert Kp to Kpp. This reaction therefore provides additional feedback between the ligand gradient and the kinases when the system is in the "on" state. This introduces one more rate constant, $c_7$ whose value is taken to be $c_6/10$. Using this value of $c_7$ does not greatly change the bistable regime (see Fig 4b) and one can therefore pick rate constants that are bistable in the stochastic simulations.

## 2.4   Stochastic reaction diffusion modeling

*Numerical simulation methods.*   The stochastic reaction-diffusion method used is the RDME. Briefly, the RDME [58–61] is an extension to the CME that adds the spatial position of each molecule into the system's state. Reaction and diffusion propensities for each molecule are calculated accounting the molecule's position. Like all kinetic Monte Carlo methods, many independent trajectories of the system are simulated and combined to calculate the probabilities. Detailed methods for all numerical techniques used in the study are given in Text S1.

*Rate constant adjustment with constant concentration of ligand.*   The CME models assume a well-stirred volume, which implies that the reactants make many collisions before taking part in a reaction [62]. When one models a system based on the RDME, the diffusion coefficient plays an important role in determining the rate of the reaction. As a result, we can no longer pick rate constants from the deterministic bistable regime and expect the proper stability behavior.

To determine parameters for the RDME simulations, we scanned across the parameters $c_1$: $0.5 - 3.0 \times 10^{-5}$, $c_2$: $1.0 - 7.0 \times 10^{-5}$, $c_3$: $1.0 - 4.0 \times 10^{-3}$, $c_4$: $1.0 - 8.0 \times 10^{-3}$, $c_5$: $1.0 - 8.0 \times 10^{-3}$ and $c_6$: $1.0 - 6.0 \times 10^{-5}$ to tune the system's bistability, starting from the CME parameters. Simulations were performed using the full three-dimensional model described above, except using constant

concentration boundary conditions with a ligand concentration of 11.4 nM. For each of Model II and III, we selected a parameter set that was bistable and was closest to having an equal probability of being in the "off" and the "on" state, *i.e.*, the system spent an approximately equal amount of time in both states. Fig S3 shows representative trajectories and PDFs for the selected RDME parameter sets. Comparing the rate constants used in the RDME models (Table S1) to CME models (Table 1), one can see that the rate constants for the RDME are much lower. This is because, unlike the CME simulations which take place in the whole volume (2.5x2.5x2.5 $\mu$m$^3$), the RDME simulations take place only in the membrane associated subvolumes. The reactions in the RDME simulations therefore take place in a more confined space and the rate constant must be lowered to keep a similar reaction rate.

## 3   Results

### 3.1   Gradient sensing in the ensemble average

In our polarization model, the spatial signal is provided by the direction of the concentration gradient of L, as shown in Fig 2. This spatial signal is passed on to the RL complex when L binds to R. From RL, the signal is eventually passed on to Kp and Kpp. We included a strong spatial positive feedback in the system, modeled by lowering the diffusion coefficients of RL and of Kp and Kpp molecules after recruitment to the membrane.

To verify that gradient simulations exhibited the desired stability characteristics, we performed RDME simulations of each model in the presence of a stochastic gradient (see Models and Methods). Model I showed the expected monostable graded response and Models II and III showed bistable behavior, switching between the "on" and "off" states Fig 5. We also performed simulations in the absence of ligand to ensure that Models II and III were still bistable, as shown in Fig 5b, and therefore exhibited spontaneous polarization. These results confirm that the parameter sets selected for the RDME model using a constant concentration of ligand are still valid for the gradient simulations.

Next, we wanted to analyze the spatial response of Kp and Kpp to a gradient in the three models. To do so we needed to quantify how closely the spatial distributions of Kp and Kpp followed the direction of the ligand gradient. To collect data for analysis, we performed RDME simulations of

14
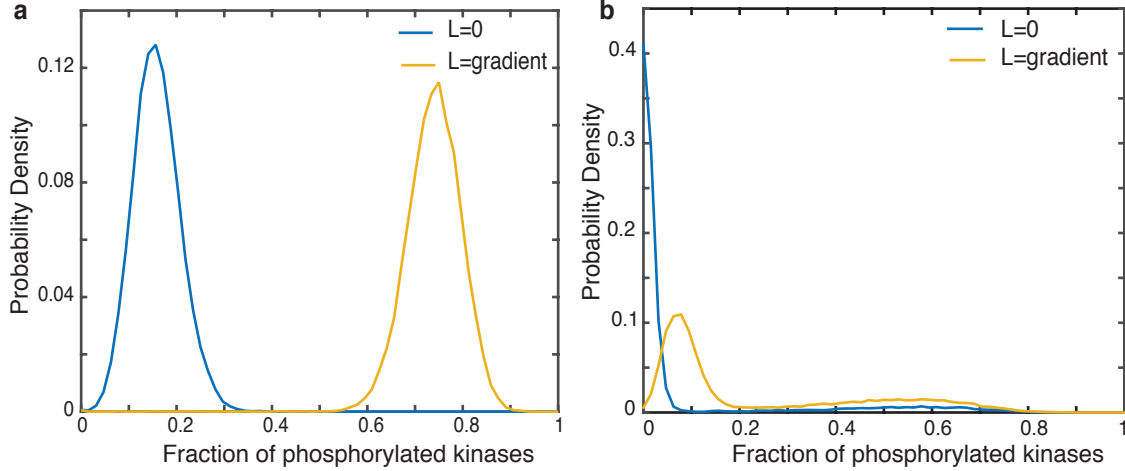
**Fig 5**: **RDME probability distributions for Models I and II.** (a) Probability distribution of fraction of Kp in Model I from 100 independent RDME simulations with (blue) zero ligand concentration or (yellow) a ligand gradient. (b) Probability distribution of fraction of phosphorylated kinases (Kp+Kpp) obtained from 50 independent RDME simulations of Model II with (blue) zero ligand or (yellow) a ligand gradient.

each of the three models. For Model I we performed 500 independent simulations and for Models II and III we performed 16,000 independent simulations, all in a stochastic gradient. Each simulation ran for 500 s of simulated time saving the state of the full lattice every 1 s. In addition we performed the same number of control simulations for each model in a constant concentration of 11.4 nM ligand, which is the minimum ligand concentration in the gradient model. Reaction rates for each of the RDME models vary and are given in Table S1.

Models II and III required significantly more simulations than Model I for the ensemble average to begin to converge. Model I is the monostable model of polarization, it does not have the second feedback link involving Kpp. Even with a low diffusion coefficient of $5.0 \times 10^{-3}$ $\mu m^2 s^{-1}$, Kp molecules in Model I do not form clusters in individual cells in the simulations. On the other hand, the presence of the second feedback link involving Kpp in Models II and III does lead to clustering of Kp and Kpp in the simulations. The properties of these clusters in individual cells are discussed below, but the clusters were relatively long-lived and moved slowly. Thus, many independent simulations were required to average out the individual clusters into an ensemble response.

To study the response for the ensemble, we first calculated the stationary probability distribution of each subvolume for each species from the individual RDME trajectories. For Models II and III we

only included time points when the system is in the "on" state. We then performed a weighted sum over the distribution to obtain the mean density for each species for each subvolume. We also calculated the stationary probability distribution and mean density from the control simulations at a constant concentration of ligand. The ratio of the densities from the gradient and control simulations is called the Enhancement Factor (EF) and corresponds to the relative increase in density in a particular subvolume due to the gradient.

Fig 6 shows the Enhancement Factor for the phosphorylated kinases (Kp for Model I and Kpp for Models II and III). It is clear from the figure that in the ensemble average the polarization of all the three models follows the gradient. In the spherical projections, the phosphorylated kinases have higher concentration near (0,0,0) and lower concentrations near (2.5,2.5,2.5). In the equirectangular projections, the concentrations of Kp and Kpp are lowest near $\theta = \frac{\pi}{4}$ and highest near $\theta = -\frac{3\pi}{4}$. Compare Fig 6d-f to the ligand-only gradient in Fig 2b. The ensemble average for Model I is much smoother than for Models II and III, which still show significant variability indicating that even after 16,000 simulations their distributions have not fully converged.

To more quantitatively define the polarization response in the three models, we calculated the EF as a function of $\Omega$. As shown schematically in Fig 2 and discussed in Models and Methods, the angle $\Omega$ is an order parameter for the membrane subvolumes with respect to the direction of the gradient, ranging from 0 where the gradient is the highest to $\pi$ where it is the lowest. Fig 7 shows the average EF value vs $\Omega$ for each of the three models as well as the ligand by itself. All three models are able to polarize along the direction of the gradient. In fact, on average all three models show identical degree of polarization, with a decrease of $\sim$15% in the concentration of phosphorylated kinases from the front to the back of the cell. However, in the ensemble average none of the models are able to recover the full range of the gradient, which is a drop of $\sim$30%.

## 3.2   Formation and behavior of polarization clusters in single cells

In the bistable Models II and III, Kp and Kpp form localized polarization clusters, primarily a single dominant cluster, when the system switches to the "on" state, an example cell is shown in Video S1. Fig 8 shows two examples of the density of a cluster of Kpp molecules during an "on" event from two Model II simulation trajectories. Each cluster is localized to a small region of the membrane,

16
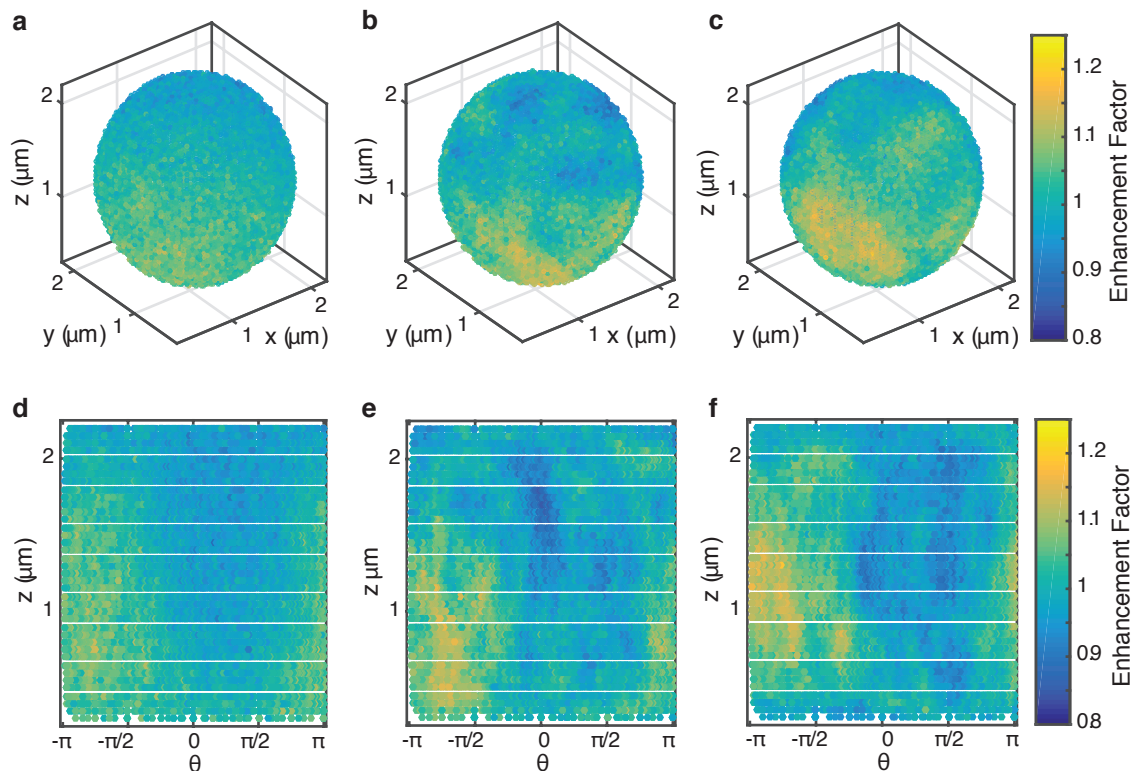
**Fig 6**: **Ensemble average response of the three models of polarization to a ligand gradient.** From left to right: Model I, Model II and Model III. (a, b, c) Spherical projection of the Enhancement Factor of Kp for Model I and Kpp for Models II and III. (d, e, f) Equirectangular projection of the same data. The ligand gradient is oriented along the vector from (0,0,0) to (2.5,2.5,2.5).
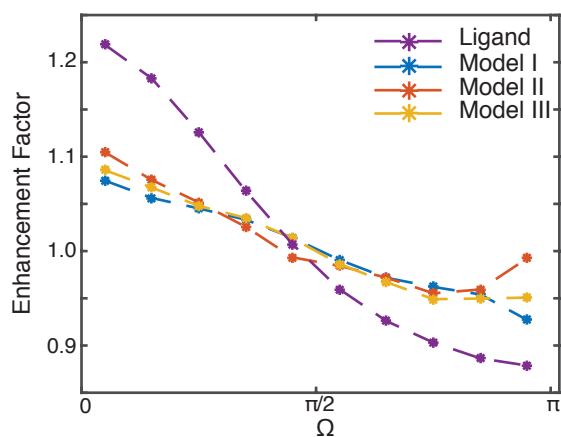


**Fig 7**: **Enhancement factor of the phosphorylated kinases vs $\Omega$.** Colors are: (blue) Model I (red) Model II and (yellow) Model III. Also shown is (purple) the ligand by itself.

with the phosphorylated kinases not spreading significantly before the system switches to the "off" state and the cluster disperses. All individual cells polarize strongly, but in a broad distribution of directions. Polarization strength is not correlated with position. Individual cells can be quite inaccurate in their polarization direction, but in the population average they align with the gradient.
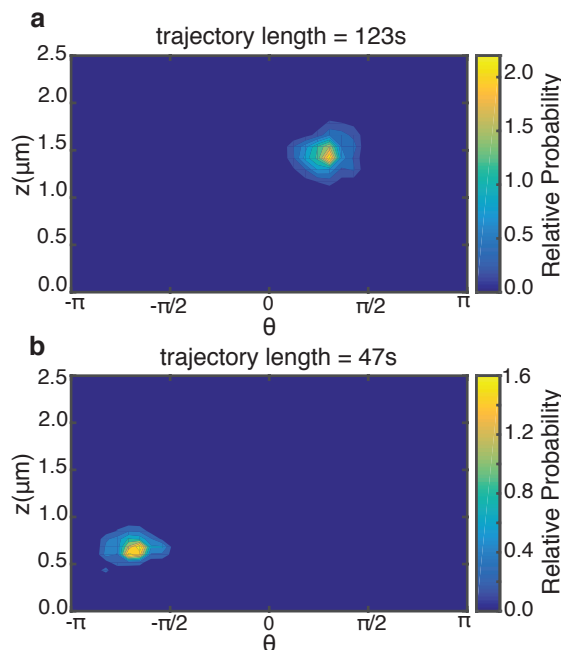


**Fig 8**: **Density of Kpp molecules during a polarization event.** (a) Kpp density during an "on" event lasting 123 s. (b) Kpp density during an "on" event lasting 47 s. Both plots are from Model II simulations.

To quantify the polarization clusters, we performed a cluster analysis of the Kpp molecules (see Models and Methods) at each time step in the "on" state for all 16,000 gradient simulations for Models II and III. Some trajectories have multiple switching events in which case we picked only the longest "on" event. We calculated the center of mass of each cluster and computed its mean square displacement (MSD) along the surface of the membrane over time, as shown in Fig 9. We fit the average MSD from the initial linear portion of the curve to a diffusion model using $\langle r^2 \rangle = 4Dt$, where $\langle r^2 \rangle$ is the MSD, D is the diffusion coefficient, and assuming two-dimensional diffusion on the surface of the membrane. For Model II D=0.0018 $\mu$m$^2$ s$^{-1}$ and for Model III D=0.0024 $\mu$m$^2$ s$^{-1}$. In both cases the diffusion of the clusters is significantly slower than of the individual Kpp molecules making up the cluster.
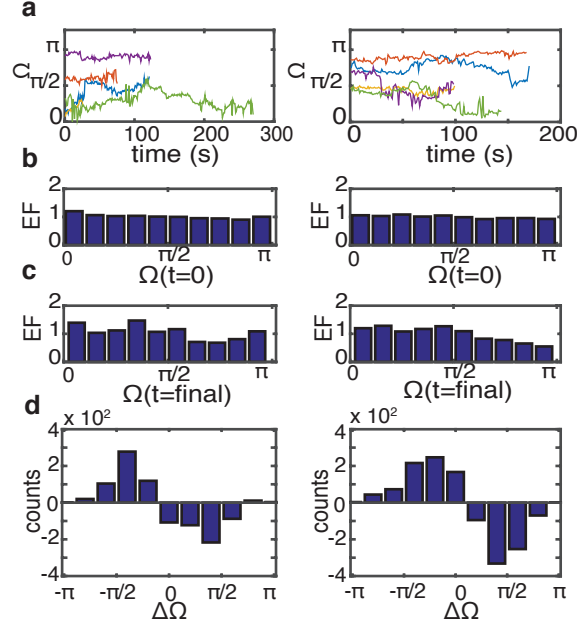
We next wondered if there was any bias in the diffusion of the clusters toward higher gradient

18
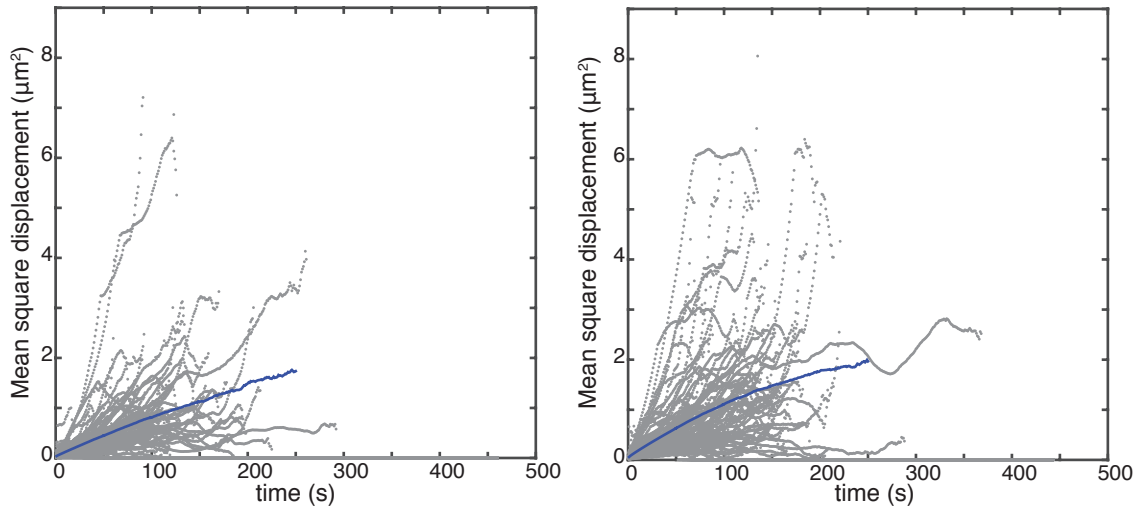
**Fig 9**: **Motion of polarization clusters over time.** The MSD of the center of mass of a cluster vs time for (a) Model II and (b) Model III. The grey curves are representative traces from 100 trajectories and the blue curves show the average of all 16,000 replicates.

regions of the cell. Fig 10a shows trajectories of some clusters and although the diffusion is slow the clusters do show drift over time. To check for bias in the drift, we compared the starting and ending $\Omega$ value for each cluster. Fig 10b+c shows that the starting $\Omega$s are distributed according to the expected EF, but the ending $\Omega$s are somewhat depleted in the range $\frac{\pi}{2}$ to $\pi$. To further check for bias, we calculated the change in $\Omega$ of each cluster, $\Delta\Omega = \Omega_{final} - \Omega_{initial}$, which gave us a distribution of $\Delta\Omega$ values. We subtracted from this distribution the $\Delta\Omega$ distribution from the control simulations to look for any differences due to the gradient. Fig 10d shows the difference between the distributions. Positive values indicate that more clusters in the gradient simulations drifted in a given direction than expected and negative values indicate fewer. There is a definite bias in the gradient simulations for more clusters to move up the gradient and fewer clusters to move down the gradient.

To further study this phenomena, we divided the clusters into those that started in the high gradient region $\Omega$=0 to $\frac{\pi}{2}$ and the low gradient region $\Omega$=$\frac{\pi}{2}$ to $\pi$. The bias was slightly more pronounced for those clusters starting in the high gradient region (see Fig S10). In addition, the data show that clusters in Model III, which have an additional positive feedback term connecting phosphorylation to the gradient, have a greater bias in their diffusion in the high gradient region.

19

**a**

C: π, π/2, 0 — time (s): 0, 100, 200, 300

C: π, π/2, 0 — time (s): 0, 100, 200

**b**

EF: 2, 1, 0 — 0, π/2, π — $\Omega(t=0)$

EF: 2, 1, 0 — 0, π/2, π — $\Omega(t=0)$

**c**

EF: 2, 1, 0 — 0, π/2, π — $\Omega(t=\text{final})$

EF: 2, 1, 0 — 0, π/2, π — $\Omega(t=\text{final})$

**d**

x 10² — counts: 4, 2, 0, -2, -4 — -π, -π/2, 0, π/2, π — $\Delta\Omega$

x 10² — counts: 4, 2, 0, -2, -4 — -π, -π/2, 0, π/2, π — $\Delta\Omega$

**Fig 10**: **Diffusion bias of polarization clusters.** Left: Model II and Right: Model III. (a) Time trajectories of representative clusters. (b) Enhancement in the distribution of $\Omega$ for the center of mass of a cluster when it forms comparing gradient to constant concentration. (c) Enhancement in the distribution of $\Omega$ for the center of mass of a cluster when it disappears comparing gradient to constant concentration. (d) Excess (positive numbers) or depleted (negative numbers) counts of the gradient model in the direction of drift $\Delta\Omega$ for the distribution of clusters, compared to the control simulations.

However, the size of the data set is not large enough to be quantitative regarding the enhanced polarization refinement in Model III.

## 3.3 Accuracy of polarization and spatial positive feedback strength

The results in the previous sections focused on the sensing of a gradient signal in the three circuit architectures. In each architecture, we included a spatial positive feedback mechanism via the low diffusion coefficients of RL, Kp, and Kpp. Spatial positive feedback in cellular responses has been attributed to many factors, including the cytoskeleton [5,53] and membrane changes [8,16] among others. To study the effect of the strength of spatial positive feedback on polarization accuracy, we ran additional simulations with higher diffusion coefficients for RL, Kp, and Kpp. We performed 16,000 independent RDME simulations of Model II, for both the gradient and control cases, at two additional diffusion coefficients: $1.0 \times 10^{-2}$ $\mu\text{m}^2\,\text{s}^{-1}$ and $5.0 \times 10^{-2}$ $\mu\text{m}^2\,\text{s}^{-1}$. The diffusion coefficient plays an important role in the stability properties of the system, see Text S1. We therefore

reparameterized the rate constants as necessary to maintain bistability in an approximately equal proportion between the "on" and the "off" states. See Table S1 for the values of the rate constants.

Fig 11 shows the EF vs $\Omega$ for all three different diffusion coefficients. The ability of the cell to accurately polarize decreases as the diffusion coefficient increases, which is a proxy for lower spatial positive feedback. With an increase in D of 2X over the original model there is still a small difference in phosphorylated kinases between the front and back of the cell on average, but with an increase of 10X the average polarization signal is gone. It is important to note that the individual cells in these models still form well-defined clusters, although not as sharp as in the original model. So the cells are still polarizing, but the accuracy of the polarization decreases with a decrease in the spatial positive feedback. The clusters diffuse too rapidly to maintain the information about the direction of the gradient.
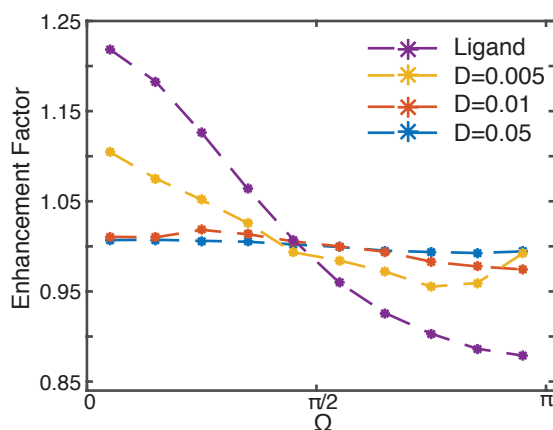


**Fig 11**: **Polarization accuracy by diffusion coefficient.** The Enhancement Factor vs $\Omega$ for Model II with three different values of D for RL, Kp, and Kpp: D=$5.0\times10^{-3}$ $\mu m^2 s^{-1}$ (yellow), D=$1.0\times10^{-2}$ $\mu m^2 s^{-1}$ (red) and D=$5.0\times10^{-2}$ $\mu m^2 s^{-1}$ (blue). The ligand is shown in purple for reference.

## 3.4  Gradient amplification in single cells

We wanted to study to what extent individual cells were able to amplify the external gradient. As stated in the introduction, this is a necessary step in cellular polarization. For Model I, we calculated the amplification by starting from the point of greatest Kp concentration in the ensemble average and calculated the concentration of Kp as a function of distance along the membrane from this point. We did the same for L for comparison purposes. As can be seen in Fig 12a, Model I is

not able to significantly amplify the gradient, in fact the gradient of Kp is slightly shallower than L.

For Models II and III, which exhibit distinct clusters, we started from the point of maximum Kpp density for 200 individual clusters and calculated the concentration of Kpp as a function of distance from this point over the entire duration of the "on" event. This calculation gave the internal gradient of Kpp in the polarized state. Fig 12a shows the concentration as a function of distance from the center of the polarization site relative to the mean concentration. The clustering in Models II and III leads to an internal gradient that is significantly stronger than the external ligand gradient. While the ligand gradient maximum is $\sim$1.3X the mean value, Models II and III produce Kpp gradients with maximum amplifications averaging $\sim$18X the mean value with a width at half-maximum of 0.25 $\mu$m. It is important to point out that even though the Kpp gradient is significantly steeper than the ligand gradient, it is not aligned precisely with the ligand gradient direction in individual cells, but rather in a distribution of directions centered on the external gradient.
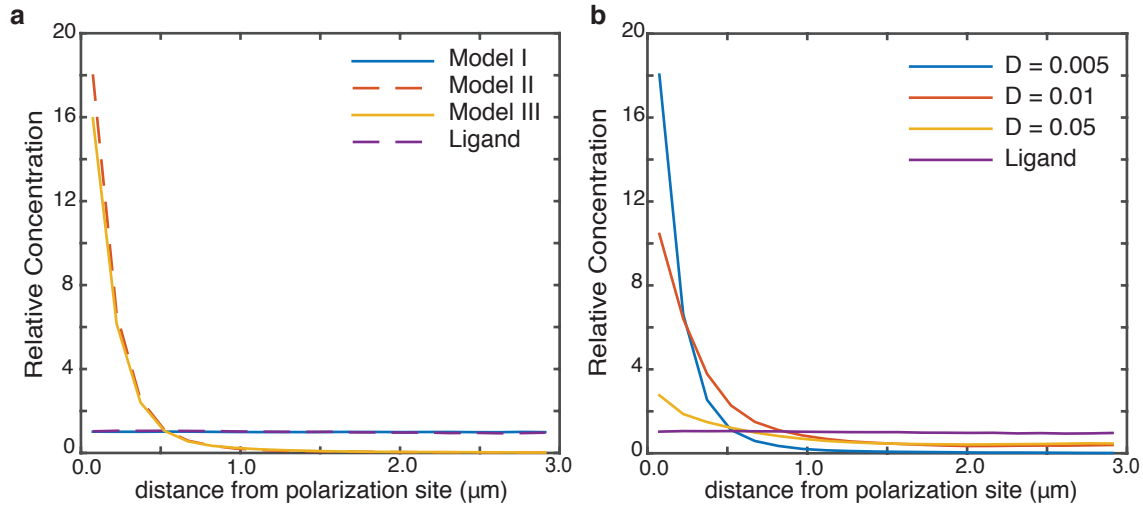


**Fig 12**: **Internal amplification of the external gradient during polarization.** (a) Relative concentration vs distance from the site of polarization from the three models: Model I (blue), Model II (red), Model III (yellow) and the ligand gradient (purple) for reference. (b) As in (a) for Model II with D=5.0×10$^{-3}$ $\mu$m$^2$ s$^{-1}$ (blue), D=1.0×10$^{-2}$ $\mu$m$^2$ s$^{-1}$ (red) and D=5.0×10$^{-2}$ $\mu$m$^2$ s$^{-1}$ (yellow). All concentrations are normalized to the average concentration in the control simulations.

We also looked at the gradient amplification of the clusters in the reduced spatial positive feedback simulations. Fig 12b shows that as D increases the maximum amplification goes down and the gradient spreads out over a larger region of the cell, becoming less point-like. Even though the simulations with increased D showed little accuracy in detecting the gradient direction,

they were still able to produce gradients of activated signaling molecules in individual cells that were stronger than the ligand gradient initiating the signal. The directional information carried by the signaling molecule gradient, though, was incorrect without strong spatial positive feedback.

## 3.5 Dependence on system size

Finally, to see if polarization occurred only when total kinase copy numbers were small and stochastic noise was large, or if it was a more general phenomenon, we carried out a set of simulations for Model II in a larger volume of $5{\times}5{\times}5\,\mu\mathrm{m}^3$. We constructed a $4\,\mu\mathrm{m}$ diameter cell in the volume and placed 500 total kinase and 2000 receptor molecules, which is in the range of molecule counts reported for the *S. cerevisiae* mating pathway [63]. We simulated 48 independent trajectories for 3000 s each (see Text S1 for simulation details). The stationary PDF for the system is shown in Figure S12, and confirms that the system is bistable; individual trajectories switched between "off" and "on" states over the course of the simulations. Though we did not collect enough simulation data to calculate the accuracy of directional response, the polarization statistics followed those of the smaller simulation volume. The cells formed polarized clusters of Kpp molecules in the "on" state with the clusters diffusing slowly on the membrane, as can be seen in Video S2. The cells showed robust polarization with an internal Kpp gradient $\sim$80X above the mean value (Figure S13). As expected, the "on" state was more stable for the larger system size, with an average duration of 179 s compared to 23 s for the smaller volume (Figure S14).

## 4 Discussion

In this study we have shown that bistability and spatial positive feedback can act in tandem to establish a strong internal cellular polarization in response to an extracellular spatial gradient. Three autophosphorylation models were analyzed, one monostable and two bistable. The monostable Model I was able to produce an internal gradient that followed the external gradient in individual cells, but was incapable of amplifying the external signal. Additionally, the direction of a cell's internal gradient experienced relatively large fluctuations due to intrinsic noise in the external gradient and the signaling pathway components.

In contrast, bistable Models II and III gave rise to strong internal amplification of the external

gradient in individual cells, resulting in a strong polarization site that was buffered from fluctuations in the external gradient. However, the tradeoff for strong polarization was inaccuracy in the polarization direction. At the population level, Models II and III recovered the gradient direction to the same degree as Model I, but individual cells in Models II and III polarized in a broad distribution of directions centered on the gradient.

Furthermore, bistable models require strong spatial positive feedback to bias the polarization site toward the direction of the gradient. The polarization clusters themselves provide some positive feedback, as the clusters diffuse more slowly than the molecules of which they are composed [33]. However, this self-feedback was not sufficiently strong to prevent the loss of information about the gradient direction. In our simulations, we needed to include an additional source of spatial positive feedback, modeled by significantly reducing the diffusion rate of the activated species, to achieve accurate gradient sensing. The individual cells still polarized without spatial feedback, but the polarization site carried no directional information. Additionally, internal gradient amplification decreased with decreasing spatial feedback and the polarization site became less sharply defined.

In our simulations with strong spatial feedback, Kpp molecules localize to form clusters, which define the polarization site. The clusters display mobility, albeit reduced in comparison to a free moving Kpp molecule. This phenomenon of a mobile cluster has also been seen in Cdc24 localization in *S. cerevisiae* [64] and in Cdc42 localization in *Schizosaccharomyces pombe* [65]. Similar to the clusters in our simulations, Hegemann *et al.* [64] have shown that the mobility of Cdc24 in yeast cells that sense a concentration gradient of $\alpha$-factor is helpful when correcting for errors in directional response as the entire cluster tries to move towards the signal direction.

The overall behavior of the system is robust to many parameter choices. While varying the values of the kinetic rate constants does lead to large changes in the ratio of the switching times between the "off" and "on" states, the polarization behavior of the system was consistent across all of the values tested as long as the system exhibited bistability. The diffusion coefficients of the activated species, though, have a large impact on the polarization process. In the limiting case in which all species have the same diffusion coefficient, polarization disappears almost instantaneously and the system likely switches to an unpolarized "on" state via traveling wave propagation [66].

Based on our work, it appears that an accurate response to a gradient signal in a bistable system can be ensured only through strong spatial positive feedback. However, too strong spatial positive feedback may limit the ability of a cell to correct initial inaccuracy or to respond to a changing gradient. In yeast strains engineered to include Bem1 in secretory vesicles, which increases the spatial positive feedback, cells lose the ability to track a gradient and instead grow in the direction of the initial guess no matter how inaccurate [5]. Additional positive and negative feedback loops are likely necessary to fine-tune the cell's ability to adjust its polarization direction.

The additional positive feedback link in Model III is an example of such a refinement. In Model II the gradient influences primarily the first step of polarization, as it dictates where a cluster forms and has less effects on the dynamics after formation. The extra positive feedback link to the gradient in Model III enables the gradient to continue to influence the cluster after it has formed, enhancing the ability of a cell to refine its initial polarization direction. In real gradient sensing pathways there will likely be feedback links to the gradient at multiple levels of the pathway.

In light of evidence that some chemosensing pathways do behave as bistable systems [9, 10] and that individual cells do display a distribution of polarization directions [5–8], we propose that bistable circuits with spatial positive feedback may be an important component of chemosensing circuits. In a conceptual model for polarization site selection, the cell constantly maintains a best guess as to the location of the gradient source. This guess represents the integrated information over some previous time window and continuously changes due to fluctuations in local concentrations of biomolecules as well as fluctuations in the gradient due to the small number of signaling molecules involved, in our simulations $9.5 \pm 3.1$ near the plasma membrane. When the bistable system switches to the "on" state, the cell locks in to its current best guess, which becomes the initial polarization site. Later refinements through additional positive and negative feedback links can serve to correct any initial errors in accuracy.

The proposed model has the advantage that it allows a cell to combine a strong all-or-none response with a direction biased toward the gradient. There is an implicit tradeoff made in such a model between the accuracy of individual cells and the strength of the spatial positive feedback, which may affect later stages of the pathway. Different species may have evolved different accuracy characteristics depending upon their particular needs. High-throughput imaging experiments characterizing the accuracy and fluctuations of individual cells polarizing in a gradient can provide

data to support and parameterize or to disprove such a model.

Finally, it is important to note that the origin of of the spatial positive feedback in real cells is unknown. Standard reaction-diffusion mechanisms appear to lose memory too quickly to be the source. The question then becomes what provides longer-term spatial memory in cells? In yeast it may be related to the cytoskeleton [5, 52, 67–69]. Cytoskeletal dynamics, particularly exocytosis, have been shown to play a key role in allowing yeast cells to track a moving gradient [5]. Cytoskeletal remodeling appears to have a memory on the order of minutes [70], which is long compared to the autocorrelation time of a reaction-diffusion process. If the cytoskeleton is the source of spatial positive feedback, new modeling techniques may be needed to accurately describe polarization accuracy as fluctuations in the cytoskeleton cannot be accurately described by reaction-diffusion dynamics [71].

The study presented here demonstrates the important connection between bistability and spatial positive feedback in chemosensing pathways and highlights the tradeoff between accuracy and amplification in individual cells. Further work to understand how such pathways balance these two competing interests will hopefully shed additional light on the capacity for cells to transduce extracellular spatial information into intracellular spatial information.

## References

[1] Swaney KF, Huang CH, Devreotes PN. Eukaryotic chemotaxis: a network of signaling pathways controls motility, directional sensing, and polarity. Annu Rev Biophys. 2010;39:265–89.

[2] Arkowitz RA. Responding to attraction: chemotaxis and chemotropism in Dictyostelium and yeast. Trends Cell Biol. 1999;9(1):20–7.

[3] Lander AD. How cells know where they are. Science. 2013;339(6122):923–7.

[4] Merlini L, Dudin O, Martin SG. Mate and fuse: how yeast cells do it. Open Biol. 2013;3(3):130008.

[5] Dyer JM, Savage NS, Jin M, Zyla TR, Elston TC, Lew DJ. Tracking shallow chemical gradients by actin-driven wandering of the polarization site. Curr Biol. 2013;23(1):32–41.

[6] Segall JE. Polarization of yeast cells in spatial gradients of alpha mating factor. Proc Natl Acad Sci USA. 1993;90(18):8332–6.

[7] Brett ME, DeFlorio R, Stone DE, Eddington DT. A microfluidic device that forms and redirects pheromone gradients to study chemotropism in yeast. Lab on a chip. 2012;12(17):3127–34.

[8] Moore TI, Tanaka H, Kim HJ, Jeon NL, Yi TM. Yeast G-proteins mediate directional sensing and polarization behaviors in response to changes in pheromone gradient direction. Mol Biol Cell. 2013;24(4):521–34.

[9] Paliwal S, Iglesias PA, Campbell K, Hilioti Z, Groisman A, Levchenko A. MAPK-mediated bimodal gene expression and adaptive gradient sensing in yeast. Nature. 2007;446(7131):46–51.

[10] Malleshaiah MK, Shahrezaei V, Swain PS, Michnick SW. The scaffold protein Ste5 directly controls a switch-like mating decision in yeast. Nature. 2010;465(7294):101–5.

[11] Maeder CI, Hink MA, Kinkhabwala A, Mayr R, Bastiaens PIH, Knop M. Spatial regulation of Fus3 MAP kinase activity through a reaction-diffusion mechanism in yeast pheromone signalling. Nat Cell Biol. 2007;9(11):1319–26.

[12] Martin SG, Arkowitz RA. Cell polarization in budding and fission yeasts. FEMS Microbiol Rev. 2014;38(2):228–53.

[13] Mogilner A, Allard J, Wollman R. Cell polarity: quantitative modeling as a tool in cell biology. Science. 2012;336(6078):175–9.

[14] Jilkine A, Edelstein-Keshet L. A comparison of mathematical models for polarization of single eukaryotic cells in response to guided cues. PLoS Comput Biol. 2011;7(4):e1001121.

[15] Goryachev AB, Pokhilko AV. Dynamics of Cdc42 network embodies a Turing-type mechanism of yeast cell polarity. FEBS Lett. 2008;582(10):1437–43.

[16] Chou CS, Moore TI, Nie Q, Yi TM. Alternative cell polarity behaviours arise from changes in G-protein spatial dynamics. IET Syst Biol. 2015;9(2):52–63.

[17] Shi C, Huang CH, Devreotes PN, Iglesias PA. Interaction of motility, directional sensing, and polarity modules recreates the behaviors of chemotaxing cells. PLoS Comput Biol. 2013;9(7):e1003122.

[18] Iglesias PA, Devreotes PN. Biased excitable networks: how cells direct motion in response to gradients. Curr Opin Cell Biol. 2012;24(2):245–53.

[19] Choi PJ, Cai L, Frieda K, Xie XS. A stochastic single-molecule event triggers phenotype switching of a bacterial cell. Science. 2008;322(5900):442–6.

[20] Leisner M, Kuhr JT, Rädler JO, Frey E, Maier B. Kinetics of genetic switching into the state of bacterial competence. Biophys J. 2009;96(3):1178–88.

[21] Eldar A, Elowitz MB. Functional roles for noise in genetic circuits. Nature. 2010;467(7312):167–73.

[22] Zong C, So LH, Sepúlveda LA, Skinner SO, Golding I. Lysogen stability is determined by the frequency of activity bursts from the fate-determining gene. Mol Syst Biol. 2010;6:440.

[23] Golding I. Decision making in living cells: lessons from a simple system. Annu Rev Biophys. 2011;40:63–80.

[24] Hao N, Yildirim N, Nagiec MJ, Parnell SC, Errede B, Dohlman HG, et al. Combined computational and experimental analysis reveals mitogen-activated protein kinase-mediated feedback phosphorylation as a mechanism for signaling specificity. Mol Biol Cell. 2012;23(19):3899–3910.

[25] McAdams HH, Arkin A. Stochastic mechanisms in gene expression. Proc Natl Acad Sci USA. 1997;94(3):814–9.

[26] Paulsson J, Ehrenberg M. Random signal fluctuations can reduce random fluctuations in regulated components of chemical regulatory networks. Phys Rev Lett. 2000;84(23):5447–50.

[27] Thattai M, van Oudenaarden A. Intrinsic noise in gene regulatory networks. Proc Natl Acad Sci USA. 2001;98(15):8614–9.

[28] Schultz D, Ben Jacob E, Onuchic JN, Wolynes PG. Molecular level stochastic model for competence cycles in Bacillus subtilis. Proc Natl Acad Sci USA. 2007;104(45):17582–7.

[29] Shahrezaei V, Swain PS. Analytical distributions for stochastic gene expression. Proc Natl Acad Sci USA. 2008;105(45):17256–61.

[30] Balázsi G, van Oudenaarden A, Collins JJ. Cellular decision making and biological noise: from microbes to mammals. Cell. 2011;144(6):910–25.

[31] Altschuler SJ, Angenent SB, Wang Y, Wu LF. On the spontaneous emergence of cell polarity. Nature. 2008;454(7206):886–9.

[32] Das J, Kardar M, Chakraborty AK. Positive feedback regulation results in spatial clustering and fast spreading of active signaling molecules on a cell membrane. J Chem Phys. 2009;130(24):245102.

[33] Jilkine A, Angenent SB, Wu LF, Altschuler SJ. A density-dependent switch drives stochastic clustering and polarization of signaling molecules. PLoS Comput Biol. 2011;7(11):e1002271.

[34] Aurell E, Sneppen K. Epigenetics as a first exit problem. Phys Rev Lett. 2002;88(4):048101.

[35] Sasai M, Wolynes PG. Stochastic gene expression as a many-body problem. Proc Natl Acad Sci USA. 2003;100(5):2374–9.

[36] Markevich NI, Hoek JB, Kholodenko BN. Signaling switches and bistability arising from multisite phosphorylation in protein kinase cascades. J Cell Biol. 2004;164(3):353–9.

[37] Hornos J, Schultz D, Innocentini G, Wang J, Walczak A, Onuchic J, et al. Self-regulating gene: An exact solution. Phys Rev E. 2005;72(5):051907.

[38] Walczak AM, Onuchic JN, Wolynes PG. Absolute rate theories of epigenetic stability. Proc Natl Acad Sci USA. 2005;102(52):18926–31.

[39] Roma DM, O'Flanagan RA, Ruckenstein AE, Sengupta AM, Mukhopadhyay R. Optimal path to epigenetic switching. Phys Rev E. 2005;71(1 Pt 1):011902.

[40] Wang X, Hao N, Dohlman HG, Elston TC. Bistability, stochasticity, and oscillations in the mitogen-activated protein kinase cascade. Biophys J. 2006;90(6):1961–78.

[41] Mehta P, Mukhopadhyay R, Wingreen NS. Exponential sensitivity of noise-driven switching in genetic networks. Phys Biol. 2008;5(2):026005.

[42] Morelli MJ, Allen RJ, Tanase-Nicola S, ten Wolde PR. Eliminating fast reactions in stochastic simulations of biochemical networks: a bistable genetic switch. J Chem Phys. 2008;128(4):045105.

[43] Wang J, Zhang K, Wang E. Kinetic paths, time scale, and underlying landscapes: a path integral framework to study global natures of nonequilibrium systems and networks. J Chem Phys. 2010;133(12):125103.

[44] Roberts E, Magis A, Ortiz JO, Baumeister W, Luthey-Schulten Z. Noise contributions in an inducible genetic switch: a whole-cell simulation study. PLoS Comput Biol. 2011;7(3):e1002010.

[45] Abel SM, Roose JP, Groves JT, Weiss A, Chakraborty AK. The membrane environment can promote or suppress bistability in cell signaling networks. J Phys Chem B. 2012;116(11):3630–40.

[46] Roberts E, Be'er S, Bohrer C, Sharma R, Assaf M. Dynamics of simple gene-network motifs subject to extrinsic fluctuations. Phys Rev E. 2015;92:062717.

[47] Beta C, Amselem G, Bodenschatz E. A bistable mechanism for directional sensing. New J Phys. 2008;10(8):083015.

[48] Semplice M, Veglio A, Naldi G, Serini G, Gamba A. A bistable model of cell polarity. PLoS One. 2012;7(2):e30977.

[49] Zuk PJ, Kochańczyk M, Jaruszewicz J, Bednorz W, Lipniacki T. Dynamics of a stochastic spatially extended system predicted by comparing deterministic and stochastic attractors of the corresponding birth-death process. Phys Biol. 2012;9(5):055002.

[50] Kochańczyk M, Jaruszewicz J, Lipniacki T. Stochastic transitions in a bistable reaction system on the membrane. J R Soc Interface. 2013;10(84):20130151.

[51] Mori Y, Jilkine A, Edelstein-Keshet L. Wave-pinning and cell polarity from a bistable reaction-diffusion system. Biophys J. 2008;94(9):3684–97.

[52] Lawson MJ, Drawert B, Khammash M, Petzold L, Yi TM. Spatial stochastic dynamics enable robust cell polarization. PLoS Comput Biol. 2013;9(7):e1003139.

[53] Orchard RC, Kittisopikul M, Altschuler SJ, Wu LF, Süel GM, Alto NM. Identification of F-actin as the dynamic hub in a microbial-induced GTPase polarity circuit. Cell. 2012;148(4):803–15.

[54] Endres RG, Wingreen NS. Accuracy of direct gradient sensing by single cells. Proc Natl Acad Sci USA. 2008;105(41):15749–54.

[55] Endres RG, Wingreen NS. Accuracy of direct gradient sensing by cell-surface receptors. Progr Biophys Mol Biol. 2009;100(1-3):33–9.

[56] Diener C, Schreiber G, Giese W, del Rio G, Schröder A, Klipp E. Yeast mating and image-based quantification of spatial pattern formation. PLoS Comput Biol. 2014;10(6):e1003690.

[57] Jin M, Errede B, Behar M, Mather W, Nayak S, Hasty J, et al. Yeast dynamically modify their environment to achieve better mating efficiency. Sci Signal. 2011;4(186):ra54.

[58] Roberts E, Stone JE, Luthey-Schulten Z. Lattice Microbes: High-performance stochastic simulation method for the reaction-diffusion master equation. J Comput Chem. 2013;34(3):245–55.

[59] Gardiner CW, McNeil K, Walls D, Matheson I. Correlations in stochastic theories of chemical reactions. J Stat Phys. 1976;14(4):307–31.

[60] Isaacson S. The reaction-diffusion master equation as an asymptotic approximation of diffusion to a small target. SIAM J Appl Math. 2009;70(1):77–111.

[61] Isaacson SA, Isaacson D. Reaction-diffusion master equation, diffusion-limited reactions, and singular potentials. Phys Rev E. 2009;80(6 Pt 2):066106.

[62] Gillespie DT. Stochastic simulation of chemical kinetics. Annu Rev Phys Chem. 2007;58:35–55.

[63] Bush A, Colman-Lerner A. Quantitative measurement of protein relocalization in live cells. Biophys J. 2013;104(3):727–36.

[64] Hegemann B, Unger M, Lee SS, Stoffel-Studer I, van den Heuvel J, Pelet S, et al. A Cellular System for Spatial Signal Decoding in Chemical Gradients. Dev Cell. 2015;35(4):458–70.

[65] Bendezú FO, Vincenzetti V, Vavylonis D, Wyss R, Vogel H, Martin SG. Spontaneous Cdc42 polarization independent of GDI-mediated extraction and actin-based trafficking. PLoS Biol. 2015;13(4):e1002097.

[66] Hat B, Kazmierczak B, Lipniacki T. B cell activation triggered by the formation of the small receptor cluster: a computational study. PLoS Comput Biol. 2011;7(10):e1002197.

[67] Chou CS, Moore TI, Chang SD, Nie Q, Yi TM. Signaling regulated endocytosis and exocytosis lead to mating pheromone concentration dependent morphologies in yeast. FEBS Lett. 2012;586(23):4208–14.

[68] Freisinger T, Klünder B, Johnson J, Müller N, Pichler G, Beck G, et al. Establishment of a robust single axis of cell polarity by coupling multiple positive feedback loops. Nat Comm. 2013;4:1807.

[69] Kelley JB, Dixit G, Sheetz JB, Venkatapurapu SP, Elston TC, Dohlman HG. RGS proteins and septins cooperate to promote chemotropism by regulating polar cap mobility. Curr Biol. 2015;25(3):275–85.

[70] Bendezú FO, Martin SG. Cdc42 explores the cell periphery for mate selection in fission yeast. Curr Biol. 2013;23(1):42–7.

[71] Roberts E. Cellular and molecular structure as a unifying framework for whole-cell modeling. Curr Opin Struct Biol. 2014;25:86–91.

Supplementary Material for

"Gradient Sensing by a Bistable Regulatory Motif Enhances Signal Amplification but Decreases Accuracy in Individual Cells"

Rati Sharma[1], Elijah Roberts[1*]

[1] Department of Biophysics, Johns Hopkins University, Baltimore, Maryland 21218, USA

* Corresponding author.
Email: eroberts@jhu.edu (ER)

# 1 Methods

## 1.1 Numerical simulation methods

### 1.1.1 Partial differential equations (PDE).

As described above, the ligand in our system diffuses from a point source and forms a concentration gradient in the diffusion volume. To calculate the gradient, we numerically simulated the diffusion equation in three dimensions:

$$\frac{\partial}{\partial t} C(\vec{r}, t) = D \cdot \nabla^2 C(\vec{r}, t)$$

using a finite difference method in MATLAB (The MathWorks, Inc.). Here, $C(\vec{r}, t)$ is the concentration of the diffusing species at the 3-dimensional position vector $\vec{r}$ at time $t$ and $D$ is the diffusion coefficient. The volume of the modeled system was 7x7x7 $\mu$m$^3$ and the lattice spacing was 0.5 $\mu$m. The source produced the ligand at a constant rate of 865 molecules/s which diffused with D=50 $\mu$m$^2$ s$^{-1}$. The simulations were performed with a time step of $4.1{\times}10^{-4}$ s to ensure stability of the method. The point source was modeled using a constant flux condition at the origin. The edges of the simulation volume were modeled to maintain a linear gradient across the boundaries. This linear gradient boundary condition approximates diffusion of a point source in an infinite volume. See Text S1 for more details.

### 1.1.2 Chemical master equation (CME).

We use chemical master equation (CME) [1] to stochastically (probabilistically) study the behavior of our system under well-stirred conditions. The CME is the stochastic equivalent to the mass-action ordinary differential equations (ODEs). The CME is actually an infinite set of ODEs that describe the time evolution of the probability for the system to have a given state [2, 3]. $\vec{x}$ is a vector containing the number of molecules for each of the $N$ species in the system. The time derivative of the probability $P_{\vec{x}}$ to be in a particular state is:

$$\frac{dP_{\vec{x}}}{dt} = \sum_r^R [-a_r(\vec{x})P_{\vec{x}}(t) + a_r(\vec{x} - \mathbf{S_r})P_{[\vec{x} - \mathbf{S_r}]}(t)].$$

$a_r(\vec{x})$ is the reaction propensity (probability per unit time) for reaction $r$ of $R$ given a state vector. $S$ is the $N \times R$ stoichiometric matrix, which contains the change in each molecule number caused by a reaction.

The CME is analytically difficult to study for systems with bimolecular reactions, such as ours. Instead, we use numerical Monte Carlo simulation, commonly known as the Gillespie algorithm or the stochastic simulation algorithm (SSA) [4]. In the algorithm, the times for the next reaction are picked randomly from an exponential distribution according to the propensities. Performing many independent trajectories, one can reconstruct the time-dependent and stationary probability density functions (PDFs) of the system. The switching times between the "on" and the "off" states can also be calculated from the individual trajectories. We carried out 100 independent CME trajectories of 10,000 s saving the state every 1 s. We used the Lattice Microbes [5] software package for performing the simulations.

### 1.1.3 Reaction diffusion master equation (RDME).

The reaction-diffusion master equation (RDME) [6–8] is an extension to the CME that adds the spatial position of each molecule into the system's state. In the RDME method, the reaction volume is subdivided into equal sized cubic subvolumes. Reactions are modeled using the standard CME within each subvolume and diffusion of molecules is modeled using first-order jump processes between neighboring subvolume. The probability for the subvolume $\nu$ to have state $\vec{x}$ is $P_{\nu_{\vec{x}}}$ and its time evolution is computed using the master equation:

$$
\begin{aligned}
\frac{dP_{\nu_{\vec{x}}}}{dt} = &\sum_\nu^V \sum_r^R [-a_r(\nu_{\vec{x}})P_{\nu_{\vec{x}}}(t) + a_r(\nu_{\vec{x}} - \mathbf{S_r})P_{[\nu_{\vec{x}} - \mathbf{S_r}]}(t)] \\
&+ \sum_\nu^V \sum_n^N \sum_\xi^{\pm \hat{i}, \hat{j}, \hat{k}} \{-d_n \nu_n P_{\nu_n}(t) + d_n[(\nu + \xi)_{n+1}]P_{\nu_{n-1},(\nu+\xi)_{n+1}}(t)\}.
\end{aligned}
$$

The first summation is the CME applied to each subvolume. The second summation describes the rate of change of the probability due to the molecules' propensity to jump to a neighboring subvolume. $\nu_n$ is the number of molecules of species $n$ in subvolume $\nu$ and $d_n$ is the diffusive propensity for a molecule of species $n$ to jump from subvolume $\nu$ to neighboring subvolumes $\nu + \xi$. The diffusive propensity $d$ is given by $D/l^2$, where $D$ is the macroscopic diffusion coefficient and $l$ is the subvolume length.

The RDME is a reasonable approximation for the Smoluchowski diffusion-limited reaction model only when certain conditions relating the average diffusion and reaction time scales hold [5, 7–10]. We have chosen the lattice spacing (50 nm) such that these conditions are met for our reaction models.

Like the CME, the RDME is analytically intractable and again we use Monte Carlo simulations to study our system. We used the next-subvolume algorithm introduced by Elf and Ehrenberg for exactly sampling the RDME [9, 11]. Simulating the RDME requires significantly more computational resources than simulating the CME. To collect the simulation data for this study, we used a custom version of the parallelized Lattice Microbes software [5] running on a high-performance computing cluster.

## 1.2 Linear gradient method for numerical integration of reaction-diffusion PDEs

In our setup of the system, a point source some distance away from the reaction volume produces ligand at a constant flux which diffuses around the source. This forms a concentration gradient of the ligand originating from the point source. We need to obtain the concentration of the ligand $c(\vec{r}, t)$ at a position $\vec{r}$ relative to the point source at time *t*.

To start, we study the problem in one dimension using the standard Laplace transform technique [12, 13]. The diffusion equation in one dimension for ligand concentration is given by

$$\frac{\partial c(x,t)}{\partial t} = D \frac{\partial^2 c(x,t)}{\partial t^2} \tag{S1}$$

where, $c(x,t)$ is the concentration at *x* at time *t*. As mentioned in the setup, we choose a constant

flux initial condition which is given by

$$-\left.\frac{\partial c(x,t)}{\partial x}\right|_{x=0} = c_s \tag{S2}$$

where $c_s$ is the constant concentration flux at the source. The boundary condition is given by

$$c(x \to \infty, t) = 0 \tag{S3}$$

which means that the concentration becomes zero infinitely far away from the source. In order to solve for $c(x,t)$, Eq (S1) is first Laplace transformed in time, which leads to a 2nd order differential equation in x given by

$$p\tilde{c}(x,p) = D\frac{\partial^2 \tilde{c}(x,p)}{\partial x^2} \tag{S4}$$

where, $\tilde{c}(x,p) \equiv \mathcal{L}\{c(x,t)\}$ is the Laplace Transform of $c(x,t)$. The boundary condition remains the same, while the initial flux condition, Eq (S2) is transformed to

$$-\left.\frac{\partial \tilde{c}(x,p)}{\partial x}\right|_{x=0} = \frac{c_s}{p} \tag{S5}$$

Solving the 2nd order differential equation Eq (S4), we get

$$\tilde{c}(x,p) = Ae^{\sqrt{p/D}x} + Be^{-\sqrt{p/D}x} \tag{S6}$$

where A and B are constants to be determined. To solve for the constants, we substitute Eq (S6) in Eq (S5) and Eq (S3). This gives

$$\left(\sqrt{\frac{p}{D}}[Ae^{\sqrt{p/D}x} + Be^{-\sqrt{p/D}x}]\right)\Bigg|_{x=0} = -\frac{c_s}{p} \Rightarrow \sqrt{\frac{p}{D}}(A-B) = \frac{-c_s}{p} \tag{S7}$$

$$\tilde{c}(x \to \infty, p) = 0 \Rightarrow A = 0 \tag{S8}$$

which in turn gives

$$
\begin{aligned}
A &= 0 \\
B &= \frac{c_s}{p}\sqrt{\frac{D}{p}}
\end{aligned}
\tag{S9}
$$

Substituting for A and B in Eq (S6) gives the exact Laplace transformed solution for $\tilde{c}(x, p)$, which is

$$
\tilde{c}(x, p) = \frac{c_s}{p}\sqrt{\frac{D}{p}}\,\mathrm{e}^{-\sqrt{p/D}x}
\tag{S10}
$$

Now to get the solution in real time, we just carry out an inverse Laplace transform of Eq (S10) in Mathematica. This gives

$$
c(x, t) = c_s\sqrt{D}\left(\frac{2\sqrt{t}}{\sqrt{\pi}}\mathrm{e}^{-\frac{x^2}{4Dt}} - \frac{x}{\sqrt{D}} + x\frac{\mathrm{Erf}(x/(2\sqrt{Dt}))}{\sqrt{D}}\right)
\tag{S11}
$$

where Erf is the error function which is defined as $\mathrm{Erf}(z) = \frac{2}{\sqrt{\pi}}\int_0^z \mathrm{e}^{-t^2}\mathrm{d}t$.

We would now like to numerically obtain the solution of the 1-D diffusion equation and compare it to the exact result, Eq (S11) as a further check. The numerical integration of the diffusion equation now has to be done on a finite lattice of size "n" and this changes the boundary conditions as we cannot have zero concentration at the boundaries of a finite lattice. We instead force the boundary and its immediate neighbor to have a linear gradient. This is invoked by creating a virtual lattice site "n+1" beyond the boundary and setting the ratio of the fluxes between the neighbors to be equal, i.e.,

$$
f(n+1)/f(n) = f(n)/f(n-1) \Rightarrow f(n+1) = f(n)^2/f(n-1)
\tag{S12}
$$

The flux of the virtual lattice site can further be approximated as

$$
c(n+1) = c(n)^2/c(n-1)
\tag{S13}
$$

where c(n) is the concentration of the ligand at the nth site. The concentration of the virtual site, c(n+1), is then used to determine the concentration at the boundary, c(n), using the finite difference method. In Fig S5, we show a plot of the concentration vs. distance (x) from the source. The blue

6

curve is the concentration obtained numerically using PDE and the red curve is from the exact analytical result from Eq (S11). The PDE solution is obtained by splitting the total length of 2 m into 100 lattice sites, with the length of each site being 0.02 m and the integration time step being 0.01 for stability. The solutions obtained from the two methods show good agreement with each other.

Although we can easily obtain the exact solution of the one dimensional diffusion equation analytically, doing the same for three dimensions is not possible. However, having shown that our numerical technique for solving the diffusion equation works in one dimension, we use the same finite difference method with linear gradient boundaries to numerically obtain the solution for the 3-D diffusion equation as well.

## 1.3 Constant gradient boundary conditions.

We have developed a novel constant gradient boundary condition for the RDME that we use here to set up and maintain a ligand gradient in the reaction volume that will provide a directional signal for polarization. To implement the boundary conditions, we create a one subvolume thick layer of virtual subvolumes around the reaction volume. Each of these virtual subvolumes has a parameter that records the mean value of the ligand concentration expected at that position in the reaction volume. For each of the real boundary subvolumes, an influx propensity is calculated from all of its neighboring virtual subvolumes using these mean ligand concentrations. This propensity is added to the total propensity for ligand to diffuse into the subvolume during the simulation. An existing ligand molecule can diffuse out of a boundary subvolume and into a virtual subvolume as usual, but it is then destroyed. Figure S2 shows a comparison of the deterministic ligand gradient with the stochastic gradient across the diagonal of the reaction volume.

Each boundary subvolume is essentially connected to one or more virtual subvolumes outside the simulation volume with a constant ligand concentration. Since these virtual subvolumes do not have fluctuations, the boundary subvolumes are lacking moments in their distribution functions. These errors will gradually disappear as the distance from the boundary increases. We analytically and numerically tested for the necessary distance until the ligand distribution in the subvolumes returns to Poissonian (see Figs. S5, S6 and S7). We use a boundary region of 5 subvolumes,

7

which in our testing is sufficient. See Text S1 for additional details.

## 1.4 Estimate of error in the variance using the RDME constant gradient boundaries

In our setup, the concentrations of the ligand at the boundaries of the reaction volume are obtained from the numerical solution of the three dimensional PDE and fed in to the RDME. These concentrations are mean values that are constant at the boundaries and have no higher moments. Therefore, when RDME simulations are performed, there might be deviations in the variance of the concentrations at the lattice sites near to the boundaries. While carrying out RDME simulations with constant gradient boundaries, it is important to ensure that the variance of the diffusing ligand converges quickly and is maintained throughout.

To this end, we looked at the spatial mean concentration and its variance in three kinds of lattices. First, we consider a periodic one-dimensional lattice with N sites, as shown in Fig S6. Each site has two neighbors facilitating exchange of molecules with the neighboring site and because of periodicity, the site N has site N-1 and site 1 as its neighbors. One expects that at steady state the mean concentrations in each of the sites would be equal and be given by c/N, where c is the total concentration of the species. The variance would also be expected to be a function of N. To determine how the variance converges with N, we find the relation between the variance and the number of lattice sites in the lattice. In the following, we calculate the mean and variance for N=3.

As shown in Fig S6, the initial concentrations of the three lattice sites are respectively $c_1$, $c_2$ and $c_3$. The molecules in each lattice site can diffuse to the neighboring one with a diffusion constant of $k$. Now, if we treat the three lattice sites as three different species, we can write down the rate equations of the concentrations as follows:

$$
\begin{aligned}
\frac{\mathrm{d}c_1}{\mathrm{d}t} &= k(c_2 + c_3) - 2kc_1 \\
\frac{\mathrm{d}c_2}{\mathrm{d}t} &= k(c_1 + c_3) - 2kc_2 \\
\frac{\mathrm{d}c_3}{\mathrm{d}t} &= k(c_1 + c_2) - 2kc_3
\end{aligned}
\tag{S14}
$$

The probability that lattice sites 1,2 and 3 have concentrations $c_1$, $c_2$ and $c_3$ at any given point

in time is given by the following chemical master equation [3]:

$$
\begin{aligned}
\frac{\mathrm{d}P_{c_1,c_2,c_3}}{\mathrm{d}t} =& k[(c_2+1)P_{c_1-1,c_2+1,c_3} - c_2 P_{c_1,c_2,c_3} + (c_3+1)P_{c_1-1,c_2,c_3+1} - c_3 P_{c_1,c_2,c_3} \\
&+ (c_1+1)P_{c_1+1,c_2-1,c_3} - c_1 P_{c_1,c_2,c_3} + (c_1+1)P_{c_1+1,c_2,c_3-1} - c_1 P_{c_1,c_2,c_3} \\
&+ (c_2+1)P_{c_1,c_2+1,c_3-1} - c_2 P_{c_1,c_2,c_3} + (c_3+1)P_{c_1,c_2-1,c_3+1} - c_3 P_{c_1,c_2,c_3}]
\end{aligned}
$$

(S15)

The rate of change with respect to time of mean concentration, $m_1 = <c_1>$ and mean square of concentration $v_1 = <c_1^2>$ in site 1 are given by

$$
\begin{aligned}
\dot{m}_1 &= \sum_{c_1}\sum_{c_2}\sum_{c_3} c_1 \dot{P}_{c_1,c_2,c_3} \\
\dot{v}_1 &= \sum_{c_1}\sum_{c_2}\sum_{c_3} c_1^2 \dot{P}_{c_1,c_2,c_3}
\end{aligned}
$$

(S16)

Similarly, one can also define $m_2$, $m_3$, $v_2$, $v_3$, $v_{12} = <c_1^2 c_2>$, $v_{23} = <c_2^2 c_3>$ and $v_{13} = <c_1^2 c_3>$, where the angular brackets denote an average over the probability distribution. Using the definitions of these ensemble averages from Eq (S16) and expanding the probabilities in these definitions using Eq (S15), we get the following rate equations of means and variances.

9

$$\begin{aligned}
\dot{m}_1 &= 2m_2 + 2m_3 - 4m_1 \\
\dot{m}_2 &= 2m_1 + 2m_3 - 4m_2 \\
\dot{m}_3 &= 2m_1 + 2m_2 - 4m_3 \\
\dot{v}_1 &= 4v_{12} + 4v_{13} - 8v_1 + 2m_1 + 2c \\
\dot{v}_2 &= 4v_{12} + 4v_{23} - 8v_2 + 4m_2 + 2m_1 + 2m_3 \\
\dot{v}_3 &= 4v_{13} + 4v_{23} - 8v_3 + 4m_3 + 2m_1 + 2m_2 \\
\dot{v}_{12} &= -8v_{12} + 2v_2 + 2v_1 + 2v_{23} + 2v_{13} - 12m_1 - 12m_2 \\
\dot{v}_{13} &= 2v_{23} + 2v_{12} + 2v_3 + 2v_1 - 8v_{13} - 2m_1 - 2m_3 \\
\dot{v}_{23} &= 2v_{13} + 2v_{12} + 2v_2 + 2v_3 - 8v_{23} - 2m_2 - 2m_3 \quad\quad \text{(S17)}
\end{aligned}$$

where c is the total concentration. After setting the L.H.S to zero at steady state, we get the solution for $m_1$, $m_2$, $m_3$, $v_1$, $v_2$ and $v_3$ as follows.

$$\begin{aligned}
m_1 &= m_2 = m_3 = c/3 \\
v_1 &= v_2 = v_3 = (c^2 + 2c)/9 \\
var_1 &= var_2 = var_3 = 2c/9 \quad\quad \text{(S18)}
\end{aligned}$$

where $var_i = v_i - m_i{}^2$ is the variance for the ith lattice.

Carrying out similar analysis for N=4, gives $m_i = c/4$ and $var_i = 3c/16$. This suggests that the mean (m), variance (var) and Fano factor (F=variance/mean) as a function of N are given by

$$\begin{aligned}
m_i(N) &= c/N \\
var_i(N) &= c(N-1)/N^2 \\
F_i(N) &= (N-1)/N \quad\quad \text{(S19)}
\end{aligned}$$

From Eq (S19), it is clear that in the limit of large N, one will recover the Poisson distribution as the Fano factor will equal 1. Fig S7 shows the variance and the deviation from Poissonian (1-F) for simulations carried over a 1D periodic lattice and its comparison with theory from Eq (S19). The figures show that the variance quickly converges as N increases and the deviation also reduces rapidly. In fact, at 5 lattice sites away from the first one, the deviation from Poissonian is 0.1. We therefore model the membrane in our reaction volume 5 subvolumes away from the boundaries of the cell and this ensures a converged variance for the concentrations of the ligand at the membrane.

We also looked at the means and variances obtained from simulations of a concentration gradient on a 1-D and 2-D lattice as shown in Figs S8 and S9. Both of these figures show that the mean is approximately equal to the variance thereby following a Poissonian distribution of ligand concentrations even for the smallest 2-D lattice size. The gradient boundary conditions for the RDME maintain the correct Poissonian distribution of concentrations across the lattice.

*Normalization of the RDME simulations.* In our model system, all the reactions take place in the membrane associated subvolumes of the cell. The membrane, which is of curved geometry, cannot be discretized onto a cubic lattice such that each subvolume has an equal number of membrane associated subvolume neighbors. Diffusion within the membrane associated subvolumes is correct in that each subvolume has the same probability of being occupied by a particular particle. However, the degree of connectivity is different for different areas of the simulation volume. Because the bistable switching is extremely sensitive to local positive feedback, a bias is introduced based on each subvolume's connectivity. In order to correct for this, we performed control simulations for each model using a constant ligand concentration of 11.4 nM. We use the ratio of the densities of Kp and Kpp in the gradient simulations to the control simulations to compare polarization in different regions of the cell. We call this ratio the "Enhancement Factor" as it is an enhancement of spatial polarization with respect to constant ligand concentration.

## 1.5   Kinase clustering calculations

During the simulations, clusters of Kp and Kpp form stochastically when the system switches to the "on" state. To identify and quantify these clusters, we first convert the 3-dimensional Cartesian

coordinates to spherical polar coordinates. Since we analyze the spatial distribution of ligand, Kp and Kpp in $\theta$-z space, we also identify the clusters in $\theta$-z space. To categorize the molecules into various clusters, we use hierarchical clustering with a cutoff distance of 25. We then calculate the center of mass of the clusters for each time step that the system is in the "on" state.

The drift of the center of mass of the clusters was calculated as a function of time. From this quantity we arrived at the mean square displacement (MSD) of the clusters on the membrane. In order to calculate the MSD, the distance that the cluster travels in a single time step was determined by first calculating the angle between the two points at the center and then calculating the distance moved (arc length) by the formula arc length = radius x angle. Doing this for all possible lengths of time and taking its square gives us the MSD of the clusters as a function of time.

## 2 Additional Results

### 2.1 Effect of kinase diffusion on bistability

A defining characteristic of reaction-diffusion master equation (RDME) models is that each species has a specific rate of diffusion within each subvolume type and between subvolumes of different types. This is in contrast to CME models where diffusion is assumed to be infinitely fast. It can be expected then that the finite diffusion coefficients in RDME models will change the stability properties of the system compared to the CME model. To study this effect, we performed 15 independent RDME simulations of Model II for each of a variety of diffusion coefficients for the phosphorylated kinase species (Kp and Kpp). Fig S11 shows how the bistability changes as D is increased. For the lowest diffusion coefficient, D=$5 \times 10^{-3}$ $\mu m^2 s^{-1}$, the system stays in the "on" state for a long time, only rarely switching "off". As D increases the system spends more and more time in the "off" state.

When phosphorylated kinases diffuse more slowly, they have increased opportunities to catalyze the phosphorylation of nearby kinases. This effect agrees with our physical understanding of the system, but creates difficulties for studying a bistable system using the RDME. We wanted to include a strong spatial positive feedback in the system, modeled by lowering the diffusion coefficient of Kp and Kpp molecules after recruitment to the membrane. To do so, while maintaining Model I as monostable and Models II and III as bistable, we had to re-parameterize the rate con-

12

stants compared to the CME. All the results in the main text are for the re-parameterized rate constants for low diffusion of $5 \times 10^{-3}$ $\mu m^2 s^{-1}$.

## 2.2   Results for large volume simulations

In order to verify that bistability, cluster formation and persistent polarization was not a phenomenon restricted to just the small system size, we carried out RDME simulations of Model II in a larger volume of 5x5x5 $\mu m^3$ as well. We carried out 48 independent RDME simulation runs of Model II with a ligand gradient. Each simulation ran for 3000 s of simulated time saving the state of the full lattice every 0.1 s. The simulations were performed in a gradient of ligand concentrations varying between 28.5 nM at (0,0,0) to 8.3 nM at (5.0,5.0,5.0) $\mu m$. The cell diameter was 4 $\mu m$. Initial species counts were: K=500 molecules, Kp=0 molecules, Kpp=0 molecules, P=130 molecules, R=2000 molecules, RL = 0 molecules. Reaction rates for this system are given in Table S2. Fig S12 gives the steady state probability distribution of the fraction of phosphorylated kinases in the system. Fig S13 gives the internal amplification of the external gradient during polarization. Finally, Fig S14 shows the difference in switching time distributions for the smaller volume simulations compared to the larger volume simulations. The larger volume simulations exist in the "on" state 10X longer than the smaller volume simulations.

## References

[1] McQuarrie D. Stochastic approach to chemical kinetics. J Appl Probab. 1967;4(3):413–78.

[2] van Kampen NG. Oxford, UK: Elsevier; 2007.

[3] Gardiner CW. New York, NY: Springer; 2004.

[4] Gillespie DT. Exact stochastic simulation of coupled chemical reactions. J Phys Chem. 1977;81(25):2340–61.

[5] Roberts E, Stone JE, Luthey-Schulten Z. Lattice Microbes: High-performance stochastic simulation method for the reaction-diffusion master equation. J Comput Chem. 2013;34(3):245–55.

[6] Gardiner CW, McNeil K, Walls D, Matheson I. Correlations in stochastic theories of chemical reactions. J Stat Phys. 1976;14(4):307–31.

[7] Isaacson S. The reaction-diffusion master equation as an asymptotic approximation of diffusion to a small target. SIAM J Appl Math. 2009;70(1):77–111.

[8] Isaacson SA, Isaacson D. Reaction-diffusion master equation, diffusion-limited reactions, and singular potentials. Phys Rev E. 2009;80(6 Pt 2):066106.

[9] Elf J, Ehrenberg M. Spontaneous separation of bi-stable biochemical systems into spatial domains of opposite phases. IEE Syst Biol. 2004;1(2):230–6.

[10] Erban R, Chapman SJ. Stochastic modelling of reaction-diffusion processes: algorithms for bimolecular reactions. Phys Biol. 2009;6(4):046001.

[11] Hattne J, Fange D, Elf J. Stochastic reaction-diffusion simulation with MesoRD. Bioinformatics. 2005;21(12):2923–4.

[12] Mehrer H. Diffusion in Solids: Fundamentals, Methods, Materials, Diffusion controlled processes. Berlin, Heidelberg: Springer-Verlag; 2007.

[13] Crank J. The mathematics of diffusion. Oxford: Clarendon Press; 1975.

**Supplementary Tables**

<table>
<thead>
<tr><th rowspan="2">Rates</th><th>Model I</th><th colspan="3">Models II and III</th></tr>
<tr><th></th><th></th><th></th><th></th></tr>
<tr><th>Units: $\mu m^2 s^{-1}$</th><th>D=0.005</th><th>D=0.005</th><th>D=0.01</th><th>D= 0.05</th></tr>
</thead>
<tbody>
<tr><td>$1^{st}$ **order**$*$</td><td></td><td></td><td></td><td></td></tr>
<tr><td>$c_5$</td><td>4.0 x $10^{-3}$</td><td>4.0 x $10^{-3}$</td><td>6.0 x $10^{-3}$</td><td>7.0 x $10^{-3}$</td></tr>
<tr><td>$2^{nd}$ **order** †</td><td></td><td></td><td></td><td></td></tr>
<tr><td>$c_0$</td><td>1.0 x $10^{-3}$</td><td>4.0 x $10^{-3}$</td><td>4.0 x $10^{-3}$</td><td>4.0 x $10^{-3}$</td></tr>
<tr><td>$c_1$</td><td>2.0 x $10^{-5}$</td><td>5.0 x $10^{-6}$</td><td>6.0 x $10^{-6}$</td><td>1.0 x $10^{-5}$</td></tr>
<tr><td>$c_2$</td><td>4.0 x $10^{-3}$</td><td>1.0 x $10^{-5}$</td><td>1.2 x $10^{-5}$</td><td>2.0 x $10^{-5}$</td></tr>
<tr><td>$c_3$</td><td>–</td><td>1.0 x $10^{-3}$</td><td>1.5 x $10^{-3}$</td><td>2.0 x $10^{-3}$</td></tr>
<tr><td>$c_4$</td><td>8.0 x $10^{-3}$</td><td>7.0 x $10^{-3}$</td><td>7.1 x $10^{-3}$</td><td>7.5 x $10^{-3}$</td></tr>
<tr><td>$c_6$</td><td>1.0 x $10^{-4}$</td><td>4.0 x $10^{-5}$</td><td>4.3 x $10^{-5}$</td><td>4.5 x $10^{-5}$</td></tr>
<tr><td>$c_7$</td><td>–</td><td>4.0 x $10^{-6}$</td><td>4.3 x $10^{-6}$</td><td>4.5 x $10^{-6}$</td></tr>
</tbody>
</table>

**Table S1**: Rate Constants for the RDME Simulations

$*$ units=$s^{-1}$; † units=$molecules^{-1}s^{-1}$

**Table S2**: Rate Constants Used in Large Volume Simulation of Model II

| Rates | Model II |
|---|---|
| Units: $\mu m^2 s^{-1}$ | D=0.005 |
| $1^{st}$ **order**$*$ | |
| $c_5$ | 2.0 x $10^{-3}$ |
| $2^{nd}$ **order** $\dagger$ | |
| $c_0$ | 5.0 x $10^{-4}$ |
| $c_1$ | 1.0 x $10^{-6}$ |
| $c_2$ | 2.0 x $10^{-6}$ |
| $c_3$ | 6.0 x $10^{-5}$ |
| $c_4$ | 2.0 x $10^{-4}$ |
| $c_6$ | 2.0 x $10^{-6}$ |

$*$ units=$s^{-1}$; $\dagger$ units=$molecules^{-1}s^{-1}$

# Supplementary Figures
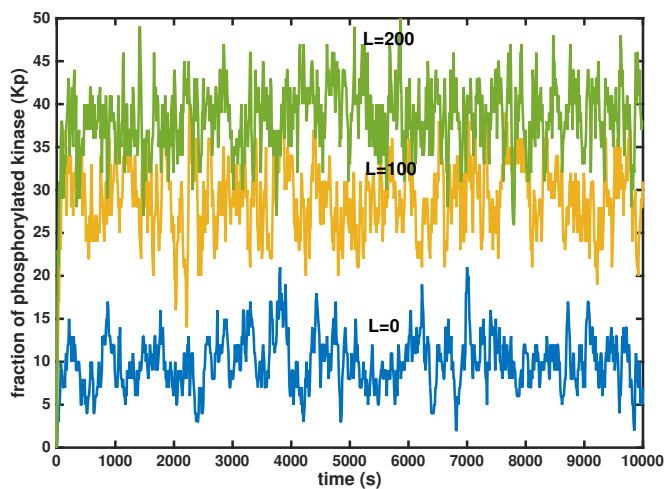


**Figure S1**: **Mean phosphorylated kinases with increasing ligand concentration.** Representative trajectories of copy numbers of phosphorylated kinases (Kp) vs. time from a CME simulation of the set of reactions in the monostable model. Initial species counts at the start of the simulation are: K=64 molecules, Kp=0 molecules, P=16 molecules, R=400 molecules, RL=0 molecules. Reaction rates are given in Table 1 of main text. Ligand copy numbers are 0 (blue), 100 (yellow), 200 (green).
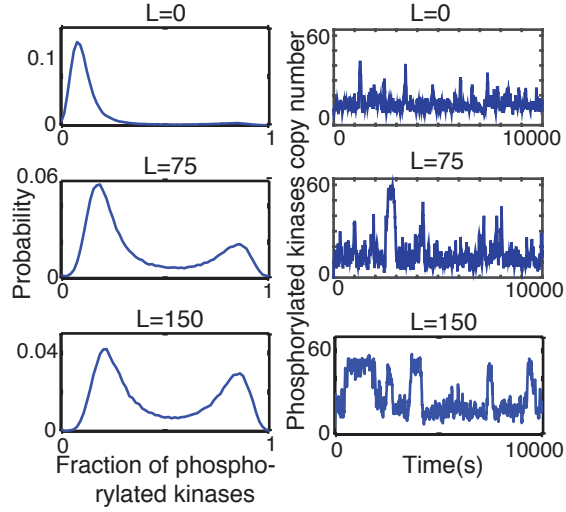
**Figure S2**: **Stochastic simulations of Model II showing bistability.** (left) Probability distribution of fraction of phosphorylated kinases (Kp+Kpp) obtained from 100 independent CME simulation runs of the set of reactions in Model II. (right) Representative trajectories showing the copy numbers of phosphorylated kinases vs. time from a CME simulation of the set of reactions in Model II. Initial species counts at the beginning of a simulation run are: K=64, Kp=0, Kpp=0, P=16, R=100, RL=0 in a volume of 2.5x2.5x2.5 $\mu$m$^3$. Ligand copy numbers are 0 (top row), 75 (middle row), 150 (bottom row).
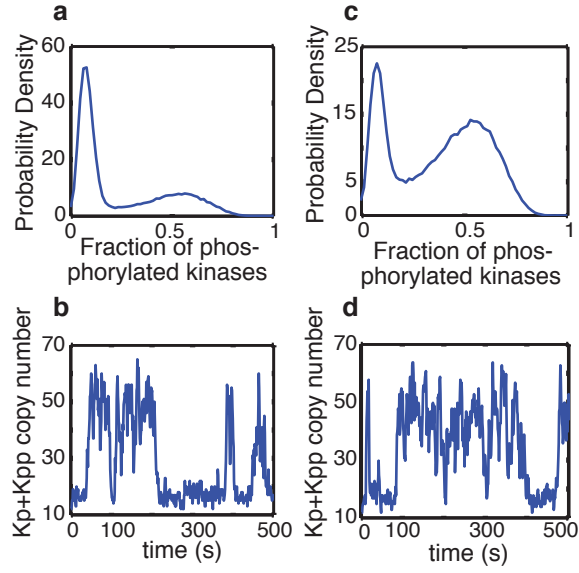
**Figure S3**: **Stochastic reaction-diffusion simulations of Model II and III with bistable parameters.** Probability distributions (top) and representative trajectories (bottom) obtained from 200 independent RDME simulations of Model II (a and b) and Model III (c and d). Initial species counts are: K=64 molecules, Kp=0 molecules, P=16 molecules, R=100 molecules, RL=0 molecules and ligand concentration=11.4 nM. Parameters are given in Table S1.
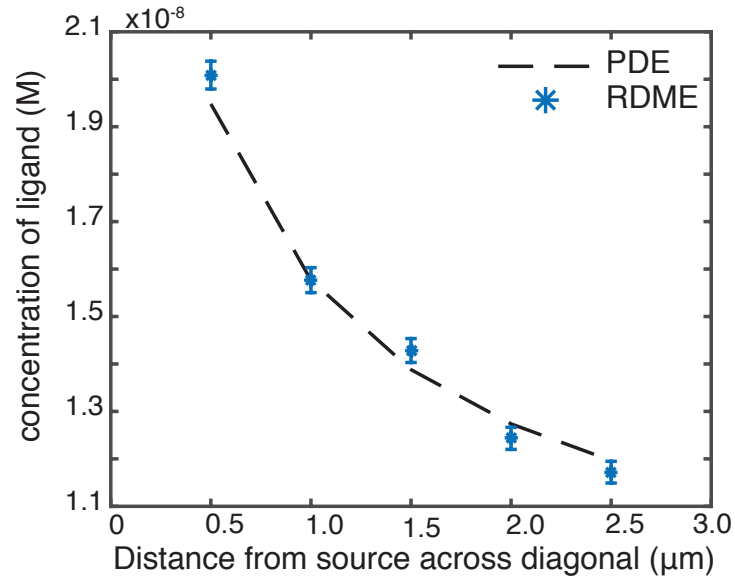
**Figure S4**: **Checking RDME simulations against numerical PDE integration.** Comparison of deterministic concentrations with that obtained from simulations in a 3D lattice of dimensions 2.5x2.5x2.5 $\mu m^3$ when boundaries have the same ligand concentrations in both. Ligand concentrations form a gradient across the diagonal of the 3D lattice.
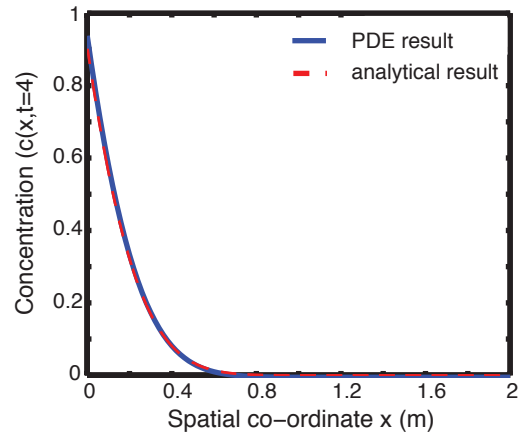
**Figure S5**: **Checking numerical PDE result against analytically obtained exact solution.** Concentration vs. distance from the source calculated by solving the partial differential equation numerically (blue) and analytically (red) for D=0.01 $m^2/s$ at time, t=4s.
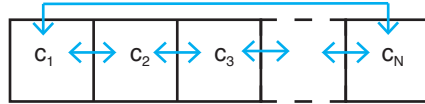
**Figure S6**: **Representation of a 1-D periodic lattice of N sites.** Here $c_1$, $c_2$ up to $c_N$ are concentrations of the species in their respective lattice sites.
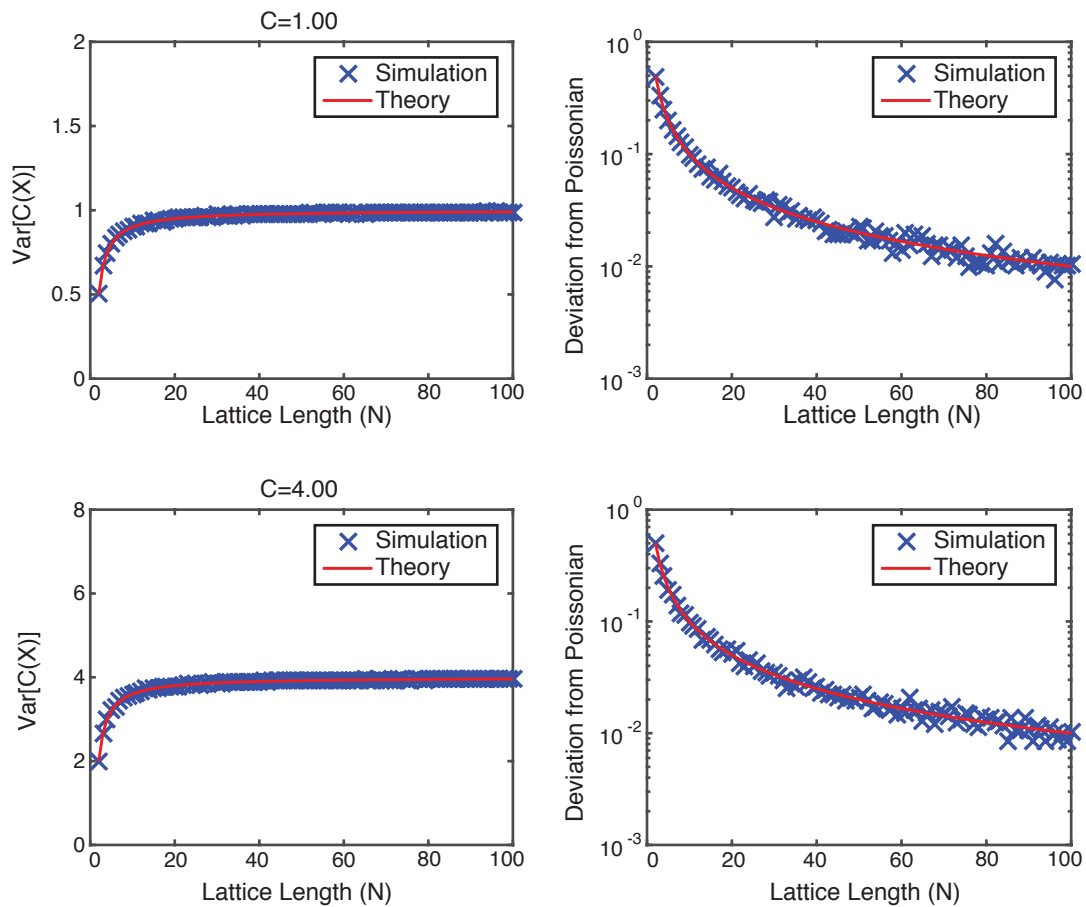
**Figure S7**: **Diffusion in a one dimensional periodic lattice.** (left) Variance and (right) deviation from Poissonian (1-F) for two different concentrations (upper) C=1 and (lower) C=4 molecules per lattice site of the diffusing species. These are also compared with the theory (red curve) obtained from Eq. (S19).
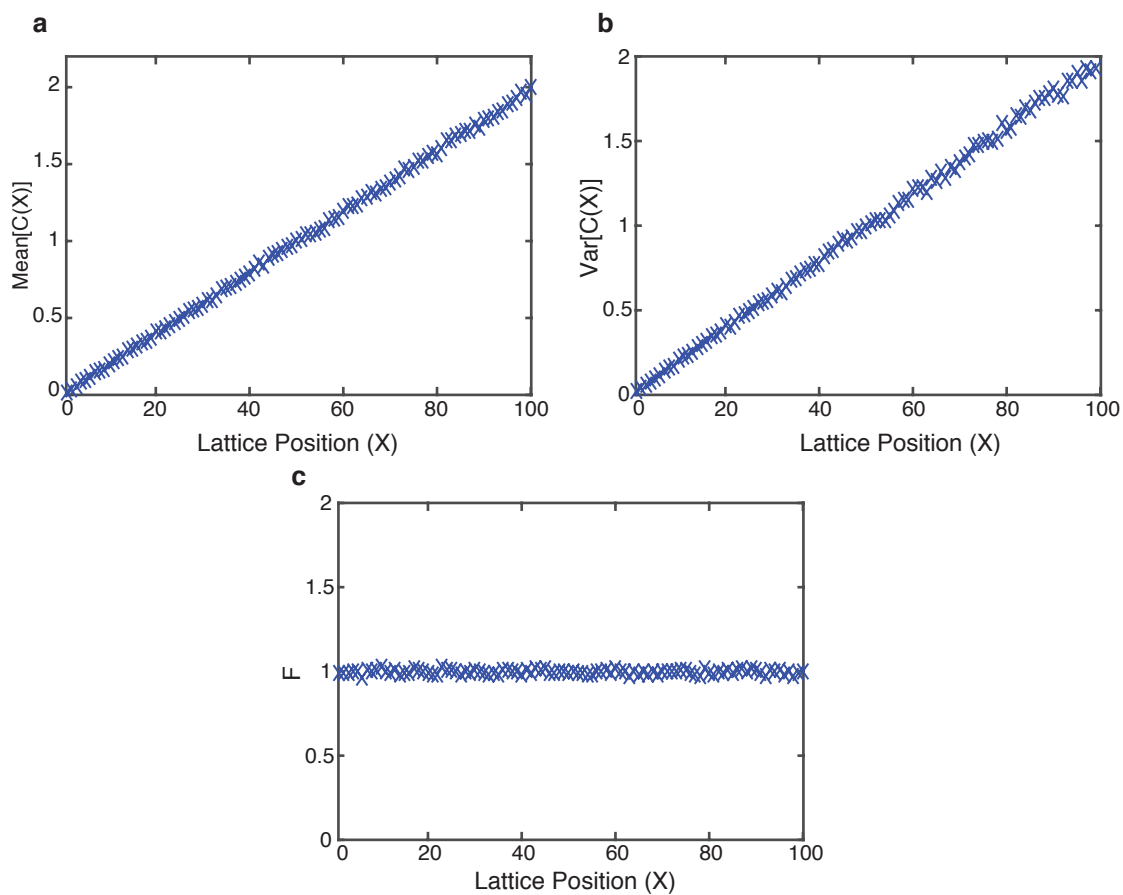
**Figure S8**: **Mean and variance as obtained from RDME simulations with constant gradient boundaries on a 1-dimensional lattice.** (a) Mean concentration (in molecules per lattice site) vs. lattice position, (b) Variance of concentration vs. lattice position, (c) Fano factor (F) vs. lattice position.
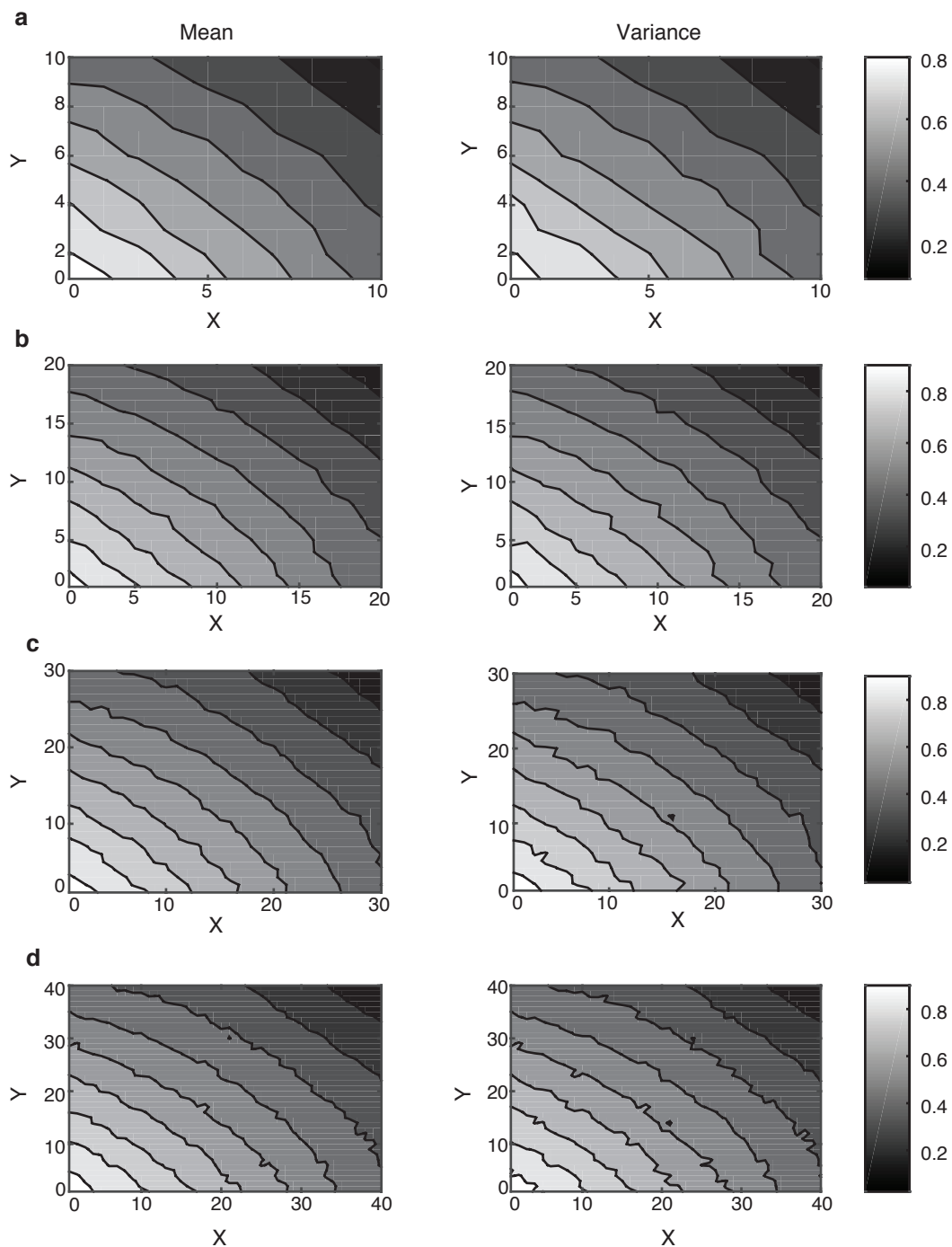
**Figure S9**: **Mean and variance as obtained from RDME simulations with constant gradient boundaries modeling a linear gradient along x and y and periodic in z.** Contour plots of mean concentration (left column) and variance in concentration (right column) for two dimensional lattices of size 10x10 (a), 20x20 (b), 30x30 (c) and 40x40 (d)
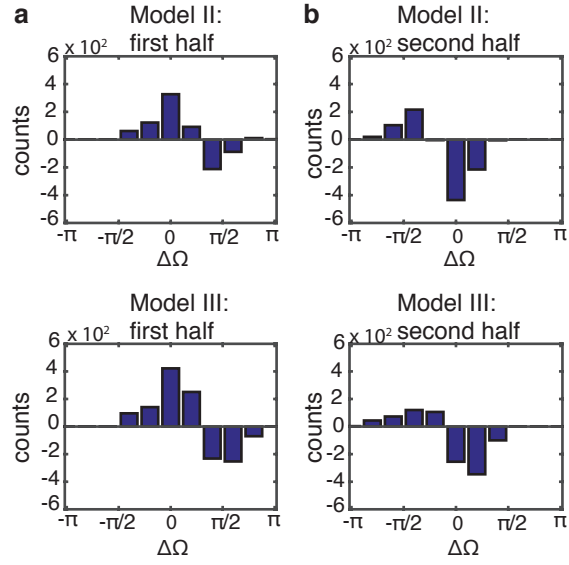
**Figure S10**: **Diffusion bias of polarization clusters.** Trajectory counts vs. $\Delta\Omega$ obtained from 16000 simulations of Models II and III for clusters of Kpp that begin to form (a) between 0 and $\pi/2$ and (b) between $\pi/2$ and $\pi$
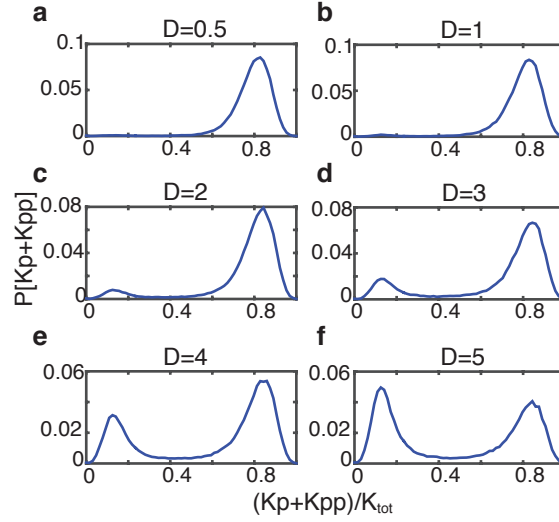
**Figure S11**: **Stability properties of RDME simulations with varying D.** Probability density for the fraction of phosphorylated kinases (Kpp) for the indicated values of D (in $\mu m^2\,s^{-1}$) for the species Kp and Kpp. Reaction rates were $c_0$=4.0×10$^{-3}$, $c_1$=5.0×10$^{-6}$ , $c_2$=1.0×10$^{-5}$, $c_3$=1.0×10$^{-3}$, $c_4$=7×10$^{-3}$, $c_5$=5×10$^{-3}$, $c_6$=4.0×10$^{-5}$ (see Table S2 for units). Other diffusion coefficients were K, P, R, and RL=5.0 $\mu m^2\,s^{-1}$ and L=50.0 $\mu m^2\,s^{-1}$. Initial species counts were: K=64, Kp,Kpp=0, P=16, R=100, RL=0.
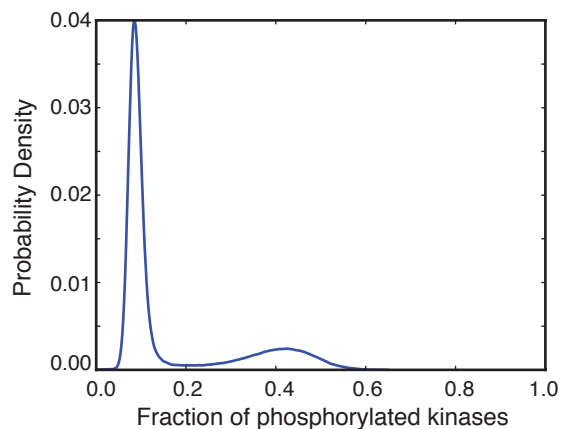
**Figure S12**: **RDME probability distributions for Model II in a large volume of 5x5x5** $\mu$m$^3$ Probability distribution of fraction of phosphorylated kinases (Kp+Kpp) obtained from 48 independent RDME simulations of Model II with a ligand gradient. Each simulation ran for 3000 s of simulated time saving the state of the full lattice every 0.1 s. The simulations were performed in a gradient of ligand concentrations varying between 28.5 nM at (0,0,0) to 8.3 nM at (5.0,5.0,5.0) $\mu$m. Initial species counts were: K=500 molecules, Kp=0 molecules, Kpp=0 molecules, P=130 molecules, R=2000 molecules, RL = 0 molecules. Reaction rates for this system are given in Table S2.
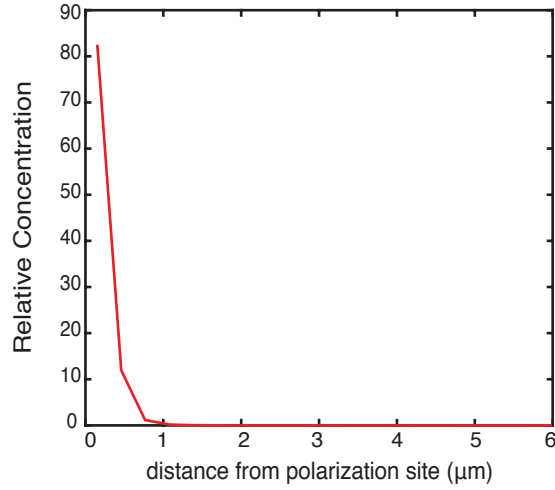
**Figure S13**: **Internal amplification of the external gradient during polarization in large volume of 5x5x5** $\mu$m$^3$ Relative concentration of Kpp vs distance from the site of polarization for Model II. The concentration of Kpp in a polarized state is normalized to the average concentration at each membrane site in the unpolarized state. Each RDME simulation ran for 3000 s of simulated time saving the state of the full lattice every 0.1 s. The simulations were performed in a gradient of ligand concentrations varying between 28.5 nM at (0,0,0) to 8.3 nM at (5.0,5.0,5.0) $\mu$m. Initial species counts were: K=500 molecules, Kp=0 molecules, Kpp=0 molecules, P=130 molecules, R=2000 molecules, RL = 0 molecules. Reaction rates for this system are given in Table S2.
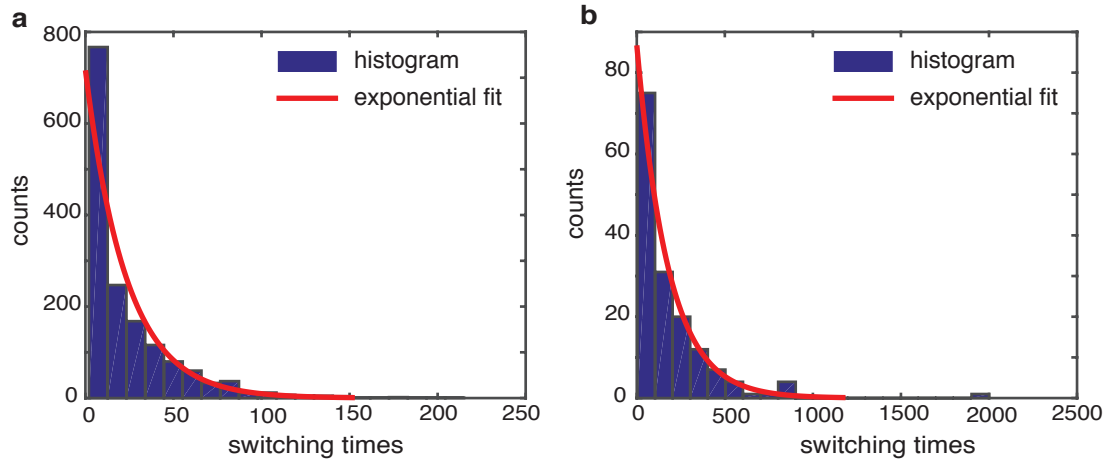
**Figure S14**: **First passage time distribution from "on" to "off" state for Model II** First passage time distribution (blue) and its exponential fit (red) for (a) smaller volume of 2.5x2.5x2.5 $\mu$m$^3$ for 200 simulation runs of Model II of 500 s each and (b) larger volume of 5x5x5 $\mu$m$^3$ for 47 simulation runs of Model II of 3000 s each.

**Video S1**: **Spatial time trajectory of Kpp for Model II in a small volume of 2.5x2.5x2.5** $\mu$m$^3$. A movie of the spatial location of Kpp on the membrane of a smaller volume recorded every 1 s from 255 s to 500 s for a 500 s simulation run. The video shows 3 switching events from "off" state to "on" state during this time span. The simulation was performed in a gradient of ligand concentrations varying between 18.5 nM at (0,0,0) to 11.4 nM at (2.5,2.5,2.5) $\mu$m. Initial species counts were: K=64 molecules, Kp=0 molecules, Kpp=0 molecules, P=16 molecules, R=100 molecules, RL = 0 molecules. Reaction rates for this system are given in Table S1.

**Video S2**: **Spatial time trajectory of Kpp for Model II in a large volume of 5x5x5** $\mu$m$^3$. A movie of the spatial location of Kpp on the membrane of a smaller volume recorded every 1 s from 1600 s to 1900 s for a 3000 s simulation run. The video shows 1 switching event from "off" state to "on" state during this time span. The simulation was performed in a gradient of ligand concentrations varying between 28.5 nM at (0,0,0) to 8.3 nM at (5.0,5.0,5.0) $\mu$m. Initial species counts were: K=500 molecules, Kp=0 molecules, Kpp=0 molecules, P=130 molecules, R=2000 molecules, RL = 0 molecules. Reaction rates for this system are given in Table S2.